

RADIATION PRESSURE SUPPORTED STARBURST DISKS & AGN FUELING

TODD A. THOMPSON,^{1,2} ELIOT QUATAERT,³ & NORMAN MURRAY^{4,5,6}
SUBMITTED TO APJ: *March 1, 2005*

ABSTRACT

We consider the structure of marginally Toomre-stable starburst disks under the assumption that radiation pressure on dust grains provides the dominant vertical support against gravity. This assumption is particularly appropriate when the disk is optically thick to its own infrared radiation, as in the central regions of Ultraluminous Infrared Galaxies (ULIRGs). We argue that because the disk radiates at its Eddington limit, the “Schmidt-law” for star formation changes in the optically-thick limit, with the star formation rate per unit area scaling as $\dot{\Sigma}_* \propto \Sigma_g / \kappa$, where Σ_g is the gas surface density and κ is the mean opacity of the disk. Our calculations further show that optically thick starburst disks have a characteristic flux, star formation rate per unit area, and dust effective temperature of $F \sim 10^{13} \text{ L}_\odot \text{ kpc}^{-2}$, $\dot{\Sigma}_* \sim 10^3 \text{ M}_\odot \text{ yr}^{-1} \text{ kpc}^{-2}$, and $T_{\text{eff}} \sim 90 \text{ K}$, respectively. We compare our model predictions with observations of ULIRGs and find good agreement.

We extend our model of starburst disks from many-hundred parsec scales to sub-parsec scales and address the problem of fueling active galactic nuclei (AGN). We assume that angular momentum transport proceeds via global torques (e.g., spiral waves, winds, or a central bar) rather than a local viscosity. We consistently account for the radial depletion of gas due to star formation and find a strong bifurcation between two classes of disk models: (1) solutions with a starburst on large scales that consumes all of the gas with little or no fueling of a central AGN and (2) models with an outer large-scale starburst accompanied by a more compact starburst on 1–10 pc scales and a bright central AGN. The luminosity of the latter models is in many cases dominated by the AGN, although these disk solutions exhibit a broad mid- to far-infrared peak from star formation. We show that the vertical thickness of the starburst disk on parsec scales can approach $h \sim r$, perhaps accounting for the nuclear obscuration in some Type 2 AGN. We also argue that the disk of young stars in the Galactic Center may be the remnant of such a compact nuclear starburst.

Subject headings: galaxies:general — galaxies:formation — galaxies:starburst — accretion, accretion disks — Galaxy: center — quasars:general

1. INTRODUCTION

Star formation in galaxies is observed to be globally inefficient; in a sample of local spiral galaxies and luminous starbursts, Kennicutt (1998) showed that only a few percent of the gas is converted into stars each dynamical time. This inefficiency may result from “feedback”: the energy and momentum injected into the interstellar medium (ISM) by star formation can in turn regulate the star formation rate in a galaxy. Models for feedback in the ISM generally invoke energy and momentum injection by supernovae and stellar winds (e.g., McKee & Ostriker 1977; Silk 1997; Efstathiou 2000). However, the momentum supplied to the ISM by the radiation from massive stars is comparable to that supplied by supernovae and stellar winds. The UV radiation from massive stars is absorbed and scattered by dust grains, which reprocess the UV emission into the IR. Because the dust grains are hydrodynamically coupled to the gas, radiation pressure on dust can help stabilize the gas against its own self-gravity and may therefore be an important feedback mechanism.

When the ISM of a galaxy is optically thick to the re-radiated

IR emission, radiative diffusion ensures that all of the momentum from the photons produced by star formation is efficiently coupled to the gas. We show that this limit is applicable on scales of hundreds of parsecs in luminous gas-rich starbursts, including Ultraluminous Infrared Galaxies (ULIRGs), the most luminous and dust enshrouded starbursts known (e.g., Genzel & Cesarsky 2000). Indeed, Scoville (2003) has already pointed out that radiation pressure on dust could plausibly be the dominant source of support against gravity in ULIRGs. We quantify this hypothesis by developing models of radiation pressure supported starburst disks.

Although radiation-pressure supported disks have not been extensively considered in the galactic context, they have been well studied in models of black hole accretion. Most notably for our present purposes, the outer parts of disks around active galactic nuclei (AGN) are expected to be dominated by radiation pressure on dust (e.g., Sirk & Goodman 2003). In the context of this paper, the distinction between the galactic disk and the AGN disk becomes somewhat unclear: if luminous AGN are fueled by gas from the cold ISM of their host galaxy, there must be a continuous transition from the star-forming “galac-

¹ Hubble Fellow² Astronomy Department & Theoretical Astrophysics Center, 601 Campbell Hall, The University of California, Berkeley, CA 94720; thomp@astro.berkeley.edu³ Astronomy Department & Theoretical Astrophysics Center, 601 Campbell Hall, The University of California, Berkeley, CA 94720; eliot@astro.berkeley.edu⁴ Canada Research Chair in Astrophysics⁵ Visiting Miller Professor, The University of California, Berkeley⁶ Canadian Institute for Theoretical Astrophysics, 60 St. George Street, University of Toronto, Toronto, ON M5S 3H8, Canada; murray@cita.utoronto.ca

tic” disk to the central black hole’s “accretion disk.” The nature of this transition, and indeed whether it occurs at all, remains uncertain. The problem is that the outer parts of AGN disks are strongly self-gravitating with a Toomre stability parameter $Q \ll 1$ (Kolykhalov & Sunyaev 1980; Shlosman & Begelman 1989; Shlosman, Begelman, & Frank 1990; Goodman 2003; Levin 2005). It is difficult to see how the disk avoids fragmenting almost entirely into stars. One possibility is that in the dense gas-rich nuclear regions of galaxies, angular momentum transport proceeds via global torques (e.g., bars, spiral waves, large-scale magnetic stresses, etc.), rather than a local viscosity (Shlosman, Frank, & Begelman 1990; Mihos & Hernquist 1996; Goodman 2003). In this case, gas may inflow sufficiently rapidly to avoid turning entirely into stars. In order to explore the fueling of a central AGN, we extend our galactic-scale disk models to smaller radii using a parameterization of the transport of angular momentum by global torques. This provides a framework for understanding the relationship between AGN activity and nuclear starbursts.

The plan for this paper is as follows. In §2, we develop a simple model of self-regulated star formation in galactic disks. We distinguish between disks that are optically thick/thin to their own IR radiation and we present models appropriate to each of these limits. Throughout §2, and in particular in §2.5, we compare our theoretical models with observations of starburst galaxies. In §3, we extend the results of §2 to include angular momentum transport and we address the problem of AGN fueling. Finally, §4 provides a discussion and summary of our conclusions, and highlights some of the predictions of our models.

2. A ONE-ZONE DISK MODEL

In this section, we construct simple dynamical models for the structure of star-forming disk galaxies. We consider two limits: (1) the “optically-thin” limit, in which the disk is optically-thick to the UV radiation produced by massive stars, but optically-thin to the re-radiated IR radiation and (2) the “optically-thick” limit, in which the disk is optically-thick to the re-radiated IR.

We begin by describing the properties of our models common to both limits. We make the clear oversimplification that the disk is a single phase medium (see, however, the brief discussions in §2.1 and Appendix B); our model thus describes only the average properties of the disk. We assume that the disk is in radial centrifugal balance with a rotation rate $\Omega = \Omega_K$, where $\Omega_K = \sqrt{2}\sigma/r$ is the Keplerian angular frequency in an isothermal potential with velocity dispersion σ . The total dynamical mass at radius r is given by $M_{\text{tot}}(r) = 2\sigma^2 r/G$ and the associated surface density is

$$\Sigma_{\text{tot}} = \frac{\sigma^2}{\pi Gr} \sim 0.6 \sigma_{200}^2 r_{\text{kpc}}^{-1} \text{ g cm}^{-2}, \quad (1)$$

where $\sigma_{200} = \sigma/200 \text{ km s}^{-1}$ and the radial scale is in units of kpc. For simplicity, we assume that the underlying potential is spherical, as would be provided by a stellar bulge or the galaxy’s dark matter halo.⁷ We further assume that the gas mass is a constant fraction $f_g = M_g/M_{\text{tot}} = \Sigma_g/\Sigma_{\text{tot}}$ of the total dynamical mass, where Σ_g is the gas surface density. Although the assumption of a constant f_g is clearly simplistic, we believe

⁷ For a Navarro, Frenk, & White (1997) dark matter profile, the dark matter mass can be significant even on the small scales of interest: $M(r) \approx 10^{10} M_{\odot} r_{\text{kpc}}^2$; this result is relatively independent of halo mass so long as $r \ll r_s$, where r_s is the scale radius of the NFW potential.

that this model captures much of the physics of interest on large scales. In §3 we relax this assumption and show that a constant gas fraction is equivalent to a constant accretion rate.

For a thin disk in a spherical potential, the equation for vertical hydrostatic equilibrium, $\partial p/\partial z = -\rho\Omega^2 z$, can be approximated as

$$p \approx \rho h^2 \Omega^2, \quad (2)$$

where h is the pressure scale height. This implies $h \approx c_s/\Omega$ where $c_s^2 = p/\rho$ is the sound speed. Throughout this paper we include turbulent pressure in our definition of the sound speed (in addition to radiation pressure and gas pressure). A term $2\pi G \Sigma_g \rho h$ should be added to the right-hand-side of equation (2) to account for the self-gravity of the disk. This leads to a multiplicative correction to equation (2) of $(1 + 2^{3/2}/Q)$, which we neglect for simplicity.

We assume that star formation in the disk is governed by local gravitational instability as described by Toomre’s Q -parameter (Toomre 1964). In particular, we argue that the disk self-regulates such that

$$Q = \frac{\kappa \Omega c_s}{\pi G \Sigma_g} = \frac{\Omega^2}{\sqrt{2}\pi G \rho}, \quad (3)$$

is maintained close to unity. In equation (3), $\kappa_\Omega^2 = 4\Omega^2 + d\Omega^2/d\ln r$ is the epicyclic frequency. The hypothesis of marginal Toomre stability has been discussed extensively in the literature (e.g., Paczynski 1978; Gammie 2001; Sirk & Goodman 2003; Levin 2005) and is based on the idea that if $Q \gg 1$ then the disk will cool rapidly and form stars, while if $Q \ll 1$ then the star formation will be so efficient that the disk will heat up to $Q \sim 1$. There is evidence for $Q \sim 1$ in the Milky Way (e.g., Binney & Tremaine 1987), local spiral galaxies (e.g., Martin & Kennicutt 2001), and starbursts such as ULIRGs (e.g., Downes & Solomon 1998).

From equation (3) it follows that the density distribution of the gas is determined solely by the local Keplerian frequency:

$$\rho = \frac{\Omega^2}{\sqrt{2}\pi G Q} = \frac{\sqrt{2}\sigma^2}{\pi G Q r^2} \Rightarrow n \sim 170 \sigma_{200}^2 r_{\text{kpc}}^{-2} Q^{-1} \text{ cm}^{-3}. \quad (4)$$

We retain the Q dependence here and below for completeness, but our assumption is that $Q \sim 1$. From the definition of Σ_g and equations (1) and (4), it then follows that

$$(h/r) = f_g Q / 2^{3/2} \quad (5)$$

and that

$$(c_s/\sigma) = f_g Q / 2. \quad (6)$$

For constant f_g and Q , h/r and c_s/σ are independent of radius. With $\sigma = 200 \text{ km s}^{-1}$, a turbulent sound speed of 10 km s^{-1} corresponds to a gas fraction of $f_{g,0.1} = f_g/0.1$. The scale height of the disk for this gas fraction is then

$$h \sim 35 f_{g,0.1} r_{\text{kpc}} \text{ pc}. \quad (7)$$

In our model, the star formation rate per unit area $\dot{\Sigma}_*$ adjusts to maintain $Q \sim 1$. We also parameterize star formation as occurring on a fraction η of the local dynamical timescale (e.g., Elmegreen 1997):

$$\dot{\Sigma}_* = \Sigma_g \Omega \eta. \quad (8)$$

Only values of $\eta \lesssim 1$ are physical. For η greater than unity the disk cannot dynamically adjust to maintain $Q \sim 1$. Although, $\dot{\Sigma}_*$ is the fundamental derived quantity, η is a useful alternative parameter that characterizes the global star formation efficiency in the disk. Observationally, η is typically ~ 0.02 in normal spiral and starburst galaxies (Kennicutt 1998).

2.1. The Optically-Thin Limit

We consider galactic disks to be “optically-thin” when the vertical optical depth to IR photons is $\lesssim 1$, but the optical depth to UV photons is greater than unity. This requires $\Sigma_g \gtrsim 2/\kappa_{\text{UV}} \sim 10^{-3} \text{ g cm}^{-2}$, where $\kappa_{\text{UV}} \sim 10^3 \text{ cm}^2 \text{ g}^{-1}$ is a characteristic UV opacity.

In our models, feedback from star formation provides the pressure support to maintain $Q \sim 1$. Sources of this pressure support include radiation pressure on dust grains, supernovae, stellar winds, and expanding HII regions. In this section we consider a simple model that relates the pressure in the ISM to the star formation rate $\dot{\Sigma}_*$ in the optically thin limit (eq. [15] below). To motivate this model, and to connect with classic treatments of the ISM (e.g., McKee & Ostriker 1977), we estimate the pressure in both the “cold” (p_c) and “hot” (p_h) phases of the ISM, focusing on the contributions from radiation pressure and supernovae. The pressure in the cold ISM can thus be written as:

$$p_c = \rho c_s^2 \sim p_{\text{rp}} + p_{\text{sn}}, \quad (9)$$

where c_s should be interpreted as a turbulent velocity and p_c as a turbulent pressure.

Because we assume that the optical depth to UV photons is greater than unity, the radiation pressure on cold gas can be related to the star formation rate by

$$p_{\text{rp}} \sim \epsilon \dot{\Sigma}_* c \quad (10)$$

where ϵ is the efficiency with which star formation converts mass into radiation ($\epsilon \sim 10^{-3}$ for a Salpeter IMF from $1 - 100 M_\odot$). Equation (10) assumes that there is no significant cancellation of oppositely directed momentum. This is uncertain, but perhaps plausible because the scattering and absorption cross sections for UV photons on dust grains are comparable and thus we expect the radiation field to be randomized on scales larger than a UV photon mean free path. Equation (10) becomes an increasingly better assumption as the disk becomes optically thick to the IR (as in starburst galaxies). In addition to radiation pressure, supernovae explosions deposit momentum into the ISM via swept-up shells of cold gas. From Thornton et al. (1998) we estimate that each supernova has an asymptotic momentum of $3 \times 10^{43} E_{51}^{13/14} n_1^{-1/4} \text{ g cm s}^{-1}$, where $E_{51} = E/10^{51} \text{ ergs}$ is the initial energy of the supernova and $n_1 = n/1 \text{ cm}^{-3}$ is the density of the ambient medium. The effective pressure of the cold ISM from supernovae — again neglecting cancellation — is thus

$$p_{\text{sn}} \sim 1.5 \times 10^8 n_1^{-1/4} E_{51}^{13/14} \dot{\Sigma}_* \sim 5 n_1^{-1/4} E_{51}^{13/14} p_{\text{rp}} \quad (11)$$

Equations (10) and (11) show that radiation pressure and supernovae contribute comparably to the pressure of the cold ISM.

Supernovae also generate a shocked hot ISM, whose pressure p_h can be estimated using the model of McKee & Ostriker (1977). Individual supernovae initially expand adiabatically to a cooling radius $R_c \sim 20 E_{51}^{0.3} n_1^{-0.4} \text{ pc}$, where a cool

dense shell forms (Chevalier 1974; Cioffi et al. 1985; Thornton et al. 1998). The subsequent remnant evolution is approximately momentum-conserving. In the absence of interaction with neighboring supernova remnants, the remnant expands to a maximum radius $R_p \sim 60 E_{51}^{0.3} n_1^{-0.2} P_{-12}^{-0.2} \text{ pc}$, where the pressure of the supernova remnant is equal to the ambient pressure (P) and $P_{-12} = P/10^{-12} \text{ ergs cm}^{-3}$. In fact, the remnant typically does not reach R_p before encountering a neighboring supernova remnant. That is, the overlap radius for supernova remnants (R_o) is $R_c < R_o < R_p$. In this model, the average pressure of the hot ISM is not known *a priori*, but can be estimated using the pressure of a supernova remnant at R_o (this assumes that there is no significant energy loss after the supernova remnants overlap and mix). Using results from Chevalier (1974), McKee & Ostriker (1977) showed that the pressure at overlap can be expressed in terms of the pressure at R_c as⁸

$$p_h \sim P_c \Psi_c, \quad (12)$$

where $\Psi_c = SV_c t_c$ is the the number of supernovae that occur in the volume $V_c \sim (4/3)\pi R_c^3$, t_c is the time for the remnant to reach R_c , and S is the supernova rate per unit volume. The time t_c has been estimated by Cox (1972) and Cioffi et al. (1985): $t_c \sim 4 \times 10^4 E_{51}^{3/14} n_1^{-4/7} \text{ yr}$ for solar metallicity. Using $P_c = E/V_c$ we find that

$$p_h \sim 10^{-12} E_{51}^{17/14} n_2^{-4/7} S_{-13} \text{ ergs cm}^{-3}, \quad (13)$$

where we have scaled the number density to a value comparable to that of the hot ISM ($n_2 = n/10^{-2} \text{ cm}^{-3}$), and the supernova rate to the Galactic value: $S_{-13} = S/10^{-13} \text{ pc}^{-3} \text{ yr}^{-1}$. Equation (13) is in reasonable agreement with observations and more detailed models of the local pressure of the ISM (McKee & Ostriker 1977; Boulares & Cox 1990).

In order to compare p_h and p_{rp} from equation (10) directly, we note that $S \sim 10^{-2} \dot{\Sigma}_*/(2h)$ with $\dot{\Sigma}_*$ in $M_\odot \text{ yr}^{-1}$ per unit area. The ratio of these two components of the pressure can then be written as

$$\frac{p_h}{p_{\text{rp}}} \sim 3 h_{100}^{-1} n_2^{-4/7} E_{51}^{17/14}, \quad (14)$$

where $h_{100} = h/100 \text{ pc}$. Because the total volume occupied by remnants with $R \leq R_c$ decreases as the density of the ISM increases, the contribution from supernovae to the total pressure decreases with increasing density. Equations (9)-(14) show that, to order of magnitude, $p_c = p_{\text{rp}} + p_{\text{sn}} \sim p_h$ for conditions appropriate to the Galaxy (as is observed).

In the luminous starbursts we focus on in this paper, the density of the ISM is much larger than in the local ISM. For example, in the inner few hundred parsecs of ULIRGs the *average* gas density reaches $10^3 - 10^4 \text{ cm}^{-3}$, comparable to the density of a local molecular cloud (e.g., Downes & Solomon 1998; see also eq. [4]). Several lines of evidence suggest that the cold molecular gas may fill a significant fraction of the volume in ULIRGs, unlike in the local ISM (Downes, Solomon, & Radford 1993; Solomon et al. 1997). The high fraction and high luminosity of radio supernovae in Arp 220 is also consistent with an environment much denser than the ISM of normal spiral galaxies (Smith et al. 1998). Taking $n \sim 10^3 \text{ cm}^{-3}$ as a characteristic value, we find that R_c is just $\sim 1 \text{ pc}$, $p_h/p_{\text{rp}} \sim 10^{-2} h_{10}^{-1}$, and that the total asymptotic thermal energy of a supernova

⁸ More carefully, Ψ_c should be raised to the 10/11-th power in equation (12) below, which we approximate as unity for simplicity.

remnant is $\sim 4 \times 10^{48}$ ergs $\ll E$ (Thornton et al. 1998). This argues against a dynamically-dominant, volume-filling hot ISM. Even in the limit of strong radiative losses, however, supernovae are still important for generating the random motion of cold gas ($p_{\text{sn}} \sim p_{\text{rp}} \gg p_h$; eq. [11]).

In the simple estimates above, all of the contributions to the pressure of the ISM scale roughly linearly with the star formation rate. Moreover, the ratio $p_{\text{rp}}/p_{\text{sn}}$ is of order unity, and while p_h/p_{rp} is of order unity in normal spiral galaxies it may be significantly smaller in the dense nuclei of the most luminous starbursts. For this reason we choose to express the effective pressure of the ISM in the “optically-thin” limit as

$$p \sim p_c = p_{\text{rp}}[1 + (p_{\text{sn}}/p_{\text{rp}})] = \epsilon \xi \dot{\Sigma}_* c, \quad (15)$$

where the last equality defines the parameter ξ . In what follows we retain the dependence of our results on ξ , but scale to $\xi \sim 1$ for the reasons given above.

Using equations (4), (6), and (15), it is straightforward to solve for the physical parameters of our disk model. The star formation rate per unit area required to support the disk with $Q \sim 1$ is given by

$$\dot{\Sigma}_* = \frac{\Sigma_g^2 \Omega^2}{4\rho \epsilon \xi c} = \frac{\Sigma_g^2 \pi G Q}{2^{3/2} \epsilon \xi c} = \frac{f_g^2 \sigma^4 Q}{2^{3/2} \pi G r^2 \epsilon \xi c}. \quad (16)$$

Scaling equation (16) for typical f_g and σ we find that

$$\dot{\Sigma}_* \sim 35 f_{g,0.5}^2 \sigma_{200}^4 r_{\text{kpc}}^{-2} \epsilon_3^{-1} \xi^{-1} Q \text{ M}_\odot \text{ yr}^{-1} \text{ kpc}^{-2} \quad (17)$$

where $\epsilon_3 = \epsilon/10^{-3}$ and $f_{g,0.5} = f_g/0.5$ is appropriate for gas-rich starbursts. The star formation rate can also be expressed in terms of the efficiency η ;

$$\eta = \frac{1}{2} \left(\frac{c_s}{\epsilon \xi c} \right) = \frac{Q}{4} \left(\frac{f_g \sigma}{\epsilon \xi c} \right) \sim 0.1 f_{g,0.5} \sigma_{200} \epsilon_3^{-1} \xi^{-1} \quad (18)$$

The second equality in equation (18) is meant to show explicitly that one may write η in terms of c_s or $f_g \sigma$ (eq. [6]). Using equation (16), the flux and luminosity of the disk viewed face-on are given by

$$F = \epsilon \dot{\Sigma}_* c^2 \sim 5 \times 10^{11} f_{g,0.5}^2 \sigma_{200}^4 r_{\text{kpc}}^{-2} Q \xi^{-1} \text{ L}_\odot \text{ kpc}^{-2} \quad (19)$$

and

$$L \equiv \pi r^2 F = \frac{f_g^2 c Q}{2^{3/2} G \xi} \sigma^4 \sim 2 \times 10^{12} f_{g,0.5}^2 \sigma_{200}^4 Q \xi^{-1} \text{ L}_\odot. \quad (20)$$

Up to logarithmic corrections, equation (20) implies that for constant f_g all radii contribute equally to the total luminosity.

The effective temperature is defined by the relation $\sigma_{\text{SB}} T_{\text{eff}}^4 = \epsilon \dot{\Sigma}_* c^2$. In the optically-thin limit, the observed dust temperature T_{dust} is related to T_{eff} by $T_{\text{dust}}^4 \sim T_{\text{eff}}^4 / (2\tau_V)$, where τ_V is the vertical optical depth to IR radiation. This relation between T_{dust} and T_{eff} assumes that the sources of UV radiation are uniformly distributed vertically throughout the disk. With equation (16),

$$T_{\text{dust}} = \left(\frac{f_g \sigma^2}{r} \frac{Q c}{2^{3/2} \kappa \xi \sigma_{\text{SB}}} \right)^{1/4} \sim 60 f_{g,0.5}^{1/4} \sigma_{200}^{1/2} (\kappa_1 \xi r_{\text{kpc}})^{-1/4} Q^{1/4} \text{ K}, \quad (21)$$

where $\kappa_1 = \kappa/1 \text{ g cm}^{-2}$ is a representative value for the IR opacity of the disk (Fig. 1) and we have assumed that an individual dust grain radiates as a blackbody.

There are several interesting properties of the disk model presented in this section. First, the efficiency of star formation required to maintain $Q \sim 1$ is $\eta \sim 0.02$ for a canonical turbulent velocity of $c_s \sim 10 \text{ km s}^{-1}$ (equivalent in our model to

having $f_g \sim 0.1$ for $\sigma \sim 200 \text{ km s}^{-1}$, as in the Galaxy). This value for η is in good agreement with observations compiled by Kennicutt (1998) (as we discuss in detail in §2.5). Second, the first two equalities in equation (16) yield $\dot{\Sigma}_* \propto \Sigma_g^2$. This Schmidt-like star formation law is somewhat steeper than the $\dot{\Sigma}_* \propto \Sigma_g^{1.4}$ favored by Kennicutt (1998), but comparable to the scaling $\dot{\Sigma}_* \propto \Sigma_g^{1.75}$ obtained by Gao & Solomon (2004) using a sample that includes more luminous starburst galaxies. Given the simplicity of the model presented here, this agreement is satisfactory. Third, for $f_g = 0.1$ and $\sigma = 200 \text{ km s}^{-1}$ the dust temperature (eq. [21]), turbulent velocity, pressure, flux, luminosity, and scale height (eq. [7]; compare with Fig. 9.25 from Binney & Merrifield 1998) are all in fair agreement with observations of the Milky Way. Thus despite its simplicity, the model presented in this section provides a useful characterization of galactic-scale star formation supported by the turbulent pressure produced by supernovae and the radiation from massive stars.

2.2. The Optically-Thick Limit

The nuclei of gas-rich starbursts are optically thick to their own infrared radiation. Radiative diffusion then ensures that radiation pressure provides the dominant vertical support against gravity. In this section we describe disk models appropriate to this limit. The vertical optical depth of the disk is given by $\tau_V = \Sigma_g \kappa/2$, where κ is the Rosseland mean opacity to dust. Evaluating this expression yields

$$\tau_V = \frac{\kappa \sigma^2 f_g}{2\pi G r} \sim 0.15 \sigma_{200}^2 f_{g,0.5} r_{\text{kpc}}^{-1} \kappa_1. \quad (22)$$

The radius at which $\tau_V = 1$ is then

$$R_{\tau_V=1} = \frac{\kappa \sigma^2 f_g}{2\pi G} \simeq 150 \kappa_1 \sigma_{200}^2 f_{g,0.5} \text{ pc} \quad (23)$$

and thus for the largest most gas-rich starbursts ($\sigma \sim 300 \text{ km s}^{-1}$ and $f_g \sim 1$) the inner $\sim 700 \text{ pc}$ are optically thick.

In the optically thick limit, the effective temperature is given by

$$\sigma_{\text{SB}} T_{\text{eff}}^4 = \frac{1}{2} \epsilon \dot{\Sigma}_* c^2, \quad (24)$$

where the factor of 1/2 arises because both the top and bottom surfaces of the disk radiate. The midplane temperature is related to the effective temperature by $T^4 \approx (3/4)\tau_V T_{\text{eff}}^4$, where the opacity $\kappa(T, \rho)$ in τ_V should be evaluated using the central temperature and mass density of the disk. The temperature dependence of the opacity is important for this problem and is discussed in the next section. For now we simply normalize κ to $1 \text{ cm}^2 \text{ g}^{-1}$.

For $\tau_V \gtrsim 1$, the radiation pressure is given by

$$p_{\text{rad}} = \frac{4\sigma_{\text{SB}}}{3c} T^4 = \frac{\sigma_{\text{SB}}}{c} \tau_V T_{\text{eff}}^4 = \frac{1}{2} \tau_V \epsilon \dot{\Sigma}_* c. \quad (25)$$

Comparing equations (15) and (25) shows that radiation pressure exceeds the turbulent pressure due to supernovae by a factor of $\sim \tau_V$ (assuming $\xi \sim 1$ for the reasons given in §2.1). Radiation pressure support will thus dominate the vertical support of compact optically-thick starbursts.

With equation (25) it is again straightforward to solve for the disk’s physical parameters, T , T_{eff} , $\dot{\Sigma}_*$, etc. in terms of our

model variables: σ , f_g , ϵ , and the radius in the disk r . The midplane temperature of the disk is

$$T = \left(\frac{f_g \sigma^2}{r} \right)^{1/2} \left(\frac{3cQ}{2^{7/2} \pi G \sigma_{\text{SB}}} \right)^{1/4} \sim 41 \sigma_{200} f_{g,0.5}^{1/2} r_{\text{kpc}}^{-1/2} Q^{1/4} \text{ K.} \quad (26)$$

and the effective temperature is

$$T_{\text{eff}} = \left(\frac{f_g \sigma^2}{r} \frac{cQ}{\sqrt{2} \kappa \sigma_{\text{SB}}} \right)^{1/4} \sim 70 \sigma_{200}^{1/2} f_{g,0.5}^{1/4} r_{\text{kpc}}^{-1/4} \kappa_1^{-1/4} Q^{1/4} \text{ K.} \quad (27)$$

For our fiducial numbers, T_{eff} is somewhat larger than T , implying that the vertical optical depth is less than unity. Our assumption that the disk is optically thick in the far IR is therefore only marginally applicable on kpc scales. It is an increasingly better assumption on smaller scales (see eqs. [22] and [23]).

The total star formation rate per unit area required to support the disk with radiation pressure is

$$\dot{\Sigma}_* = \frac{\sqrt{2} f_g Q \sigma^2}{\epsilon \kappa c} \sim 400 f_{g,0.5} \sigma_{200}^2 Q r_{\text{kpc}}^{-1} \kappa_1^{-1} \epsilon_3^{-1} \text{ M}_\odot \text{ yr}^{-1} \text{ kpc}^{-2}. \quad (28)$$

Integrating, we derive the total star formation rate:

$$\dot{M}_* = \frac{2^{3/2} \pi f_g Q \sigma^2 r}{\epsilon \kappa c} \sim 3000 f_{g,0.5} \sigma_{200}^2 r_{\text{kpc}} Q \epsilon_3^{-1} \kappa_1^{-1} \text{ M}_\odot \text{ yr}^{-1}. \quad (29)$$

Note that if the disk is optically-thick ($2 \times \tau_V \sim 1$), the observed flux is only from half of the disk and therefore the observationally inferred star formation rate would be one-half of the true total star formation rate (given in eqs. [28] & [29]).

The star formation efficiency η is

$$\eta = \frac{\pi G Q r}{\kappa \epsilon c \sigma} \sim 1 r_{\text{kpc}} \sigma_{200}^{-1} \epsilon_3^{-1} \kappa_1^{-1} Q. \quad (30)$$

For $r \lesssim R_{\tau_V=1}$ we see that η is < 1 . It follows that the disk can adjust to maintain $Q \sim 1$ on sub-kpc scales. In addition, we find that the ratio of the cooling timescale to the orbital timescale is much less than unity, so the disk should self-regulate to maintain $Q \sim 1$ (see Appendix B).

Finally, the surface brightness of the disk viewed face-on is

$$F = \frac{f_g Q c \sigma^2}{\sqrt{2} \kappa r} \sim 3 \times 10^{12} f_{g,0.5} \sigma_{200}^2 r_{\text{kpc}}^{-1} Q \kappa_1^{-1} \text{ L}_\odot \text{ kpc}^{-2} \quad (31)$$

and the total luminosity for a single side of the disk is

$$L = \frac{\sqrt{2} \pi f_g Q c r \sigma^2}{\kappa} \sim 2 \times 10^{13} f_{g,0.5} \sigma_{200}^2 r_{\text{kpc}} Q \kappa_1^{-1} \text{ L}_\odot. \quad (32)$$

Equations (27)-(32) show that the observable properties of the disk depend sensitively on the magnitude of the opacity. In particular, the star formation rate per unit area is proportional to $\Sigma_g^2 / \tau_V \sim \Sigma_g / \kappa$ (eq. [28]). Therefore, in regions of the disk where the opacity is low, there must be more star formation to maintain $Q \sim 1$. Conversely, where the optical depth is high, less star formation is required. The functional dependence of $\dot{\Sigma}_*$ in the optically-thick limit should be compared with the equation (16), which shows that in the optically-thin limit $\dot{\Sigma}_* \propto \Sigma_g^2$. Therefore, the “Schmidt-law” for star formation changes in the dense optically-thick inner regions of starburst galaxies.

Equation (31) can be rewritten as

$$\frac{L}{M} = \frac{F}{\dot{\Sigma}_{\text{tot}}} = \frac{\pi Q G c f_g}{\sqrt{2} \kappa} = \frac{2 \pi G c h}{\kappa r} \sim 10^3 \frac{f_{g,0.5} Q}{\kappa_1} \frac{\text{L}_\odot}{\text{M}_\odot}. \quad (33)$$

⁹ The factor 2π rather than the more standard 4π in equation (50) is because the luminosity in equation (32) is only from 1/2 of the disk.

The third equality above is the classical Eddington limit, modified by the factor $(h/r) \propto f_g$.⁹ This way of expressing the flux highlights the fact that each disk annulus radiates at its local Eddington limit. The value derived here for the luminosity per unit mass from the disk is similar to that estimated by Scoville (2003), who argues that this limit is observed in both young star clusters such as M51 and ULIRGs such as Arp 220 (see also Scoville et al. 2001). Note that for a given gas fraction, the mass-to-light ratio is proportional to the dust opacity and is therefore metallicity dependent.

2.3. Opacity Dependence

Figure 1 shows the Rosseland mean opacity as a function of temperature for several densities using the publicly available opacities of Semenov et al. (2003) and Bell & Lin (1994). There are two important features. First, for temperatures $T \lesssim 100 - 200$ K, the opacity is essentially independent of density and can be approximated by $\kappa = \kappa_0 T^2$, with $\kappa_0 \simeq 2.4 \times 10^{-4} \text{ cm}^2 \text{ g}^{-1} \text{ K}^{-2}$. The scaling of κ with T^2 follows from the fact that the dust absorption cross section scales as $\lambda^{-\delta}$ with $\delta \rightarrow 2$ in the Rayleigh limit (Pollack et al. 1985). The normalization κ_0 is somewhat uncertain and depends on grain physics and the dust-to-gas ratio; the latter may vary systematically as a function of radius and metallicity in starburst disks. In fact, in our own galaxy there is evidence that the dust-to-gas ratio increases within the central few kpc (Sodroski et al. 1997). In what follows we set $\kappa_{-3.6} = \kappa_0 / 2.4 \times 10^{-4} \text{ cm}^2 \text{ g}^{-1} \text{ K}^{-2}$ and retain the scaling with κ_0 . The second important feature of Figure 1 is the dramatic decrease in the opacity for $10^3 \text{ K} \lesssim T \lesssim 10^4 \text{ K}$, the “opacity gap.” Here, the temperature is larger than the sublimation temperature of dust, but smaller than the temperature at which hydrogen is significantly ionized.

Equation (26) shows that, even for the largest galaxies with the highest gas fractions, the temperature at $\sim 0.1 - 1$ kpc is $\lesssim 100$ K, and so the opacity on large scales can be approximated by $\kappa = \kappa_0 T^2$. We may then eliminate the opacity dependence from the disk properties derived above. Remarkably, because $T \propto \Sigma_g^{1/2}$ and $\dot{\Sigma}_* \propto \Sigma_g / \kappa$, with $\kappa \propto T^2$ we find that the star formation rate per unit area, the effective temperature, and flux are all independent of virtually all model parameters:

$$\dot{\Sigma}_* = \left(\frac{2^{9/2} \pi G \sigma_{\text{SB}} Q}{3 \epsilon^2 \kappa_0^2 c^3} \right)^{1/2} \sim 10^3 \epsilon_3^{-1} \kappa_{-3.6}^{-1} Q^{1/2} \text{ M}_\odot \text{ yr}^{-1} \text{ kpc}^{-2} \quad (34)$$

$$F = \left(\frac{2^{5/2} \pi G \sigma_{\text{SB}} Q c}{3 \kappa_0^2} \right)^{1/2} \sim 10^{13} \kappa_{-3.6}^{-1} Q^{1/2} \text{ L}_\odot \text{ kpc}^{-2}, \quad (35)$$

and

$$T_{\text{eff}} = \left(\frac{2^{5/2} \pi G Q c}{3 \kappa_0^2 \sigma_{\text{SB}}} \right)^{1/8} \sim 88 \kappa_{-3.6}^{-1/4} Q^{1/8} \text{ K}. \quad (36)$$

In particular, note that neither $\dot{\Sigma}_*$, F , nor T_{eff} depend on r , σ , or f_g . Our model thus predicts that starburst disks have roughly constant flux and effective temperature over a range of radii.

The constancy of these disk observables follows from three ingredients: (1) the disk is supported by radiation pressure and $\tau_V \gtrsim 1$, (2) the disk self-regulates with $Q \sim 1$, and (3) $\kappa \propto T^2$ at low T . Above $T \sim 100 - 200$ K, κ ceases to increase monotonically with T (see Fig. 1) and equations (34)-(36) no longer

hold. Because $T \propto r^{-1/2}$ (eq. [26]), the temperature exceeds ~ 200 K at a radius $R_{200} \sim 40\sigma_{200}^2 f_{g,0.5} T_{200}^{-2} Q^{1/2}$ pc. This radius should be compared with the radius at which $\tau_V = 1$. Using the $\kappa \propto T^2$ scaling, we find that

$$R_{\tau_V=1} = \sigma^2 f_g \left(\frac{3c\kappa_0^2 Q}{2^{11/2} \sigma_{\text{SB}} (\pi G)^3} \right)^{1/4} \sim 250 \sigma_{200}^2 f_{g,0.5} \kappa_{-3.6}^{1/2} Q^{1/4} \text{pc} \quad (37)$$

(compare with eq. [23]). Therefore, we expect $\dot{\Sigma}_*$, T_{eff} , and F to be roughly constant in the radial range $R_{200} \lesssim r \lesssim R_{\tau_V=1}$, \sim hundreds of parsecs for fiducial parameters.

For completeness we note that the scaling for the dust temperature in the optically-thin limit can also be re-written using $\kappa \propto T^2$ (eq. [21]):

$$T_{\text{dust}} \sim 60 f_{g,0.5}^{1/6} \sigma_{200}^{1/3} r_{\text{kpc}}^{-1/6} \kappa_{-3.6}^{-1/6} Q^{1/6} \xi^{-1/6} \text{K.} \quad (38)$$

The weak scaling with model parameters in equation (38) implies that the dust temperature should not vary significantly from system to system, as appears to be observed (e.g., Yun & Carilli 2002).

2.4. Combining the Optically-Thin & Optically-Thick Limits

The optically-thin and optically-thick limits can be combined by expressing the pressure as

$$p = \epsilon \dot{\Sigma}_* c \left(\frac{1}{2} \tau_V + \xi \right) \quad (39)$$

using the full temperature-dependent opacity curve (Fig. 1). Recall that in the limit $\tau_V \gg 1$ equation (39) describes true radiation pressure support while in the limit $\tau_V \ll 1$ it describes turbulent support with contributions from supernovae and radiation pressure. Because the opacity depends on temperature, we must connect the central temperature with the effective temperature in order to solve equation (39). By interpolating between the optically-thin and optically-thick regimes we obtain (see also Sirk & Goodman 2003)

$$T^4 = \frac{3}{4} T_{\text{eff}}^4 \left(\tau_V + \frac{2}{3\tau_V} + \frac{4}{3} \right). \quad (40)$$

In the optically-thick limit, equations (39) and (40) combine to yield $(4\sigma_{\text{SB}}/3c)T^4 \sim p$, whereas in the optically-thin limit $(4\sigma_{\text{SB}}/3c)2\tau_V T^4 \sim p$. In solving equations (39) and (40), we find multiple solutions because of the complicated temperature dependence of the opacity. In Appendix B, we address the thermal and viscous stability of these solutions. We argue that there is a single stable physical low-temperature solution and focus on this solution throughout the paper.

Figure 2 shows the numerically calculated structure of our disk models for $\sigma = 200$ km s $^{-1}$ and with $f_g = 0.03$ and 1. There are three regimes to notice in Figure 2. First, at large radii the disk is optically thin. In this region $\dot{\Sigma}_* \propto r^{-2}$ and $\eta \sim \text{const}$ (see §2.1). At smaller radii the disk becomes optically thick. There is then a range of radii ($50 \lesssim r \lesssim 300$ pc for $f_g = 1$) where $\dot{\Sigma}_*$ and T_{eff} are roughly constant, in good agreement with the estimates in §2.3. Note that where the disk is optically thin $T_{\text{dust}}^4 \sim T_{\text{eff}}^4/(2\tau_V)$. At very small radii $\sim 1 - 10$ pc the opacity decreases dramatically when dust grains sublimate (the “opacity gap”; Fig. 1). In this region the disk becomes optically thin, and the star formation rate required to maintain $Q \sim 1$ increases significantly (see also Sirk & Goodman 2003). We present a detailed discussion of this part of the disk in §3 and Appendix A, but note here that it is unphysical to assume that the gas fraction is constant throughout the region where the star formation rate increases so markedly.

2.5. Comparison With Observations

Following Kennicutt (1998), Figure 3 shows a plot of $\dot{\Sigma}_*$ as a function of $\Sigma_g/\tau_{\text{dyn}}$, where $\tau_{\text{dyn}} = 2\pi/\Omega$ is the dynamical time in the disk (ideally measured at the half-light radius). This plot essentially quantifies the star formation efficiency $\eta \equiv \dot{\Sigma}_*/(\Sigma_g \Omega)$ (see eq. [8]). The data on local spirals (crosses) and local starbursts (open triangles) are taken from Kennicutt (1998). To this we have added local ULIRG data from Downes & Solomon (1998) and high-redshift ULIRG data from Tacconi et al. (2005). The caption to Figure 3 describes the data in more detail. Note that there are significant uncertainties in determining $\dot{\Sigma}_*$ and Σ_g for the most compact starbursts, primarily because the appropriate half-light and half-mass radii are difficult to determine. CO half-power radii are often used for this purpose, but there is evidence that star formation is often significantly concentrated with respect to the CO (see the discussion of ULIRGs below).

Superimposed on the data in Figure 3 we plot our theoretical predictions for $\sigma = 200$ km s $^{-1}$ and several values of f_g . For small values of $\Sigma_g/\tau_{\text{dyn}}$, the disk is optically thin and $\eta \sim \text{constant}$, as is observed (see eq. [18]). For more compact starbursts, the disk becomes optically thick and we predict that $\dot{\Sigma}_*$ ceases to increase linearly with $\Sigma_g/\tau_{\text{dyn}}$. Instead, Figure 3 shows that $\dot{\Sigma}_*$ is significantly *smaller* than a straightforward extrapolation of the Kennicutt law would suggest. This is because when the disk is optically thick, radiation pressure support is larger than that due to supernovae or stellar winds by a factor of $\sim \tau_V$ (see eq. [25]). The efficient radiation pressure support implies a smaller star formation rate at a fixed value of $\Sigma_g/\tau_{\text{dyn}}$. The observations shown in Figure 3 are so sparse in the high surface density limit that higher resolution observations are clearly needed to quantitatively test these predictions.

Our results can also be compared to an empirical surface brightness limit for starbursts found by Meurer et al. (1997), who argued that starburst fluxes satisfy $F \lesssim 2 \times 10^{11} L_{\odot} \text{ kpc}^{-2}$, which corresponds to $\dot{\Sigma}_* \lesssim 13 \epsilon_3^{-1} M_{\odot} \text{ yr}^{-1} \text{ kpc}^{-2}$. Our calculations suggest that Meurer et al.’s limit does not represent a fundamental limit to the surface brightness of starburst galaxies. Interestingly, we do find a characteristic surface brightness of $F \sim 10^{13} L_{\odot} \text{ kpc}^{-2}$ ($\sim 50 \times$ Meurer et al.’s limit) for radiation pressure supported starbursts, though this applies only when the dust temperature is $T \lesssim 100 - 200$ K and can be exceeded in other circumstances (see Figs. 2 & 3).

2.5.1. Application to ULIRGs

To focus the discussion, we emphasize the application to Arp 220, a prototypical ULIRG. Arp 220 consists of two merging nuclei separated by about 350 pc (Graham et al. 1990). The total FIR luminosity of the system is $\sim 10^{12} L_{\odot}$. The 2–10 keV X-ray luminosity is only $\sim 3 \times 10^9 L_{\odot}$, however, and the column density of X-ray absorbing material must exceed 10^{25} cm^{-2} if an obscured AGN is to contribute significantly to the bolometric luminosity (Iwasawa et al. 2001). Thus, there is little evidence for an energetically important AGN. The detection

of numerous radio supernovae also supports a starburst origin for most of the radiation from Arp 220 (Smith et al. 1998).

The stellar velocity dispersion of Arp 220 is $\sim 165 \text{ km s}^{-1}$ (Genzel et al. 2001) and it has an extended CO disk with a scale of $\sim 500 \text{ pc}$ (Downes & Solomon 1998). Perhaps $\sim 1/2$ of the luminosity, however, appears to come from two counter-rotating nuclear disks, each of which is $\sim 100 \text{ pc}$ in extent (e.g., Sakamoto et al. 1999; Soifer et al. 1999; Downes & Solomon 1998). Radio observations also show that nearly all of the radio flux — presumably associated with supernovae and star formation — originates within $\sim 50 - 100 \text{ pc}$ of the double nuclei (Condon et al. 1991). The total mass in each of the compact nuclear disks is $\sim 2 \times 10^9 M_\odot$, with a large gas fraction of $f_g \sim 0.5$ (Downes & Solomon 1998). The nuclear region of Arp 220 is optically thick to at least $25 \mu\text{m}$ and the inferred blackbody temperature at this wavelength is $\gtrsim 85 \text{ K}$ (Soifer et al. 1999). The estimated gas mass and radius of the disk imply a surface density of $\Sigma_g \approx 10 \text{ g cm}^{-2}$, suggesting that the nuclear region is probably optically thick even in the FIR (as implied by eq. [23]).

In the optically-thick limit, with $\kappa \propto T^2$, our model predicts a radiative flux of $\sim 10^{13} L_\odot \text{ kpc}^{-2}$ (eq. [35]), in good agreement with the flux inferred for the compact nuclei in Arp 220 (see also Fig. 4 discussed below). Our model also predicts an effective temperature of $\sim 88 \text{ K}$ for this very compact emission (eq. [36]), in agreement with that estimated by Soifer et al. (1999). Lastly, we note that for a gas fraction of $f_g \sim 0.5$ and a velocity dispersion of $\sigma \sim 200 \text{ km s}^{-1}$, our model predicts a sound speed (i.e., turbulent velocity or line-width) of $c_s \sim 50 \text{ km s}^{-1}$, similar to that observed in CO by Downes & Solomon (1998).

In their study of CO emission from ULIRGs, Downes & Solomon (1998) identified compact nuclear starbursts in Mrk 273 and Arp 193 with properties similar to those discussed above for Arp 220. More directly, Condon et al. (1991) imaged the radio emission in the 40 brightest galaxies in the IRAS Bright Galaxy Sample. They resolved the emission in nearly all of the sources (36/40) and found sizes $\sim 100 \text{ pc}$. They further showed that the radio emission from ULIRGs — correcting for free-free absorption in some cases — places them on the FIR-radio correlation of starburst galaxies. This is consistent with starbursts contributing significantly to the bolometric power of these sources. In the absence of direct FIR imaging of ULIRGs, the radio sizes from Condon et al. (1991) are currently the best estimate of the size of the nuclear starbursts in these systems. Figure 4 shows a histogram of the number of sources at a given flux inferred using the FIR luminosity and the size of the resolved radio source from Condon et al. (1991). The histogram shows a peak centered on a flux $\sim 10^{13} L_\odot \text{ kpc}^{-2}$. This characteristic ‘observed’ flux is consistent with the predictions of our optically thick disk models (eq. [35]).¹⁰

An alternative way to present this data is shown in Figure 5, where we plot the inferred flux as a function of the size of the resolved radio source. Superimposed on the data we plot the predictions of our disk models for $\sigma = 200 \text{ km s}^{-1}$ and several f_g (solid lines), and for $\sigma = 300 \text{ km s}^{-1}$ and $f_g = 1$ (dashed line). The latter is a plausible upper limit to the emission expected in our starburst models. This Figure demonstrates the excellent agreement between our models and the observations

for $f_g \sim 0.3 - 1$. The data are also consistent with the increase in flux we predict for more compact starbursts. Taken together, the results of Figures 4 and 5 provide strong support for our interpretation of ULIRGs as Eddington-limited starbursts.

The characteristic flux $\sim 10^{13} L_\odot \text{ kpc}^{-2}$ found in Figure 4 is equivalent to a blackbody temperature of $\sim 90 \text{ K}$ (eq. [36]). This is noticeably larger than the typical color temperature of $\sim 60 \text{ K}$ inferred from the FIR spectra of ULIRGs. Another way to state this result is that using the observed FIR spectra and luminosity, the blackbody size of the FIR emitting region is typically larger (by a factor of few) than the radio sizes observed by Condon et al. (1991). This is likely because the compact nuclei of many ULIRGs are optically thick even at $\sim 30 \mu\text{m}$, so that radiative diffusion degrades the $\sim 90 \text{ K}$ emission and ensures that the FIR size can be larger than the true size of the nuclear starburst. This interpretation requires sufficient obscuring gas at large radii, but also that star formation in this gas does not dominate the bolometric power of the source (or else the radio source would be more extended than is observed). In our models we find that if the gas fraction in the nuclear region increases at small radii, as Downes & Solomon (1998) infer for several systems, then most of the luminosity is produced near the radius where $\tau_V \sim 1$, rather than in the extended optically thin portion of the disk at larger radii.

To conclude this section, we compare our model predictions with the observations of high-redshift ULIRGs (“submm sources”) presented in Tacconi et al. (2005). Tacconi et al. describe CO observations of 4 high- z systems with the PdBI. They find an average velocity dispersion of $\sigma \simeq 290 \pm 35 \text{ km s}^{-1}$, gas fraction of $f_g \simeq 0.4 \pm 0.2$, and half-power radius for CO of $R_{\text{CO}} \simeq 1.6 \pm 0.3 \text{ kpc}$. The global properties of the disks in the high- z ULIRGs appear to be scaled up versions of their local counterparts, with luminosities $\sim 10 \times$ higher and CO-disks $\sim 3 \times$ larger, implying comparable fluxes and $\dot{\Sigma}_*$. For the f_g and σ inferred from the observations, we predict that the radius at which the disk becomes optically-thick to its own IR radiation is $R_{\tau_V=1} \simeq 400 - 500 \text{ pc}$. Our disk calculations yield a total luminosity of $1 - 2 \times 10^{13} L_\odot$ and a flux that varies from $6 \times 10^{11} L_\odot \text{ kpc}^{-2}$ at 1.6 kpc to $10^{13} L_\odot \text{ kpc}^{-2}$ at 200 pc . We also predict a dust temperature of $\sim 57 \text{ K}$ at $\sim 1.6 \text{ kpc}$, a sound speed of $c_s \sim 60 \text{ km s}^{-1}$, and a gas surface density of $\Sigma_g \sim 0.8 \text{ g cm}^{-2}$. These predictions are in excellent agreement with the observations of Tacconi et al.: $L \sim 10^{13} L_\odot$, $F \sim 10^{12} L_\odot \text{ kpc}^{-2}$, $c_s \simeq 95 \pm 30 \text{ km s}^{-1}$ and $\Sigma_g \simeq 0.6 \pm 0.1 \text{ g cm}^{-2}$. As discussed extensively above, in local ULIRGs the nuclear starbursts appear significantly concentrated with respect to the large-scale CO disks. It remains to be seen if the same is true in their high-redshift counterparts (Chapman et al. 2004 find radio sizes of $\sim 3 \text{ kpc}$ in several systems, suggesting that star formation may be more extended in some high redshift ULIRGs).

3. DISK MODELS WITH ACCRETION

In the previous section we considered the properties of large-scale starburst disks with constant gas fraction. In this section we address the problem of AGN fueling by connecting our kpc-scale starburst disks with AGN disks on sub-parsec scales. This requires a consistent treatment of the gas fraction, which must evolve with radius as a result of star formation.

¹⁰ Note that our conclusions are not significantly changed if only (say) $\sim 1/2$ of the bolometric power is produced by the compact nuclei resolved in the radio (as some models of Arp 220 suggest; e.g., Soifer et al. 1999).

On large scales, models with constant gas fraction are equivalent to models with a constant mass accretion rate. To see this, consider a Shakura-Sunyaev accretion disk with viscosity $\nu = \alpha c_s h$. The mass accretion rate in such a disk is given by

$$\dot{M} = 2\pi\nu\Sigma_g \left| \frac{d\ln\Omega}{d\ln r} \right| = \frac{2^{3/2}\alpha h^3\Omega^3}{GQ} \left| \frac{d\ln\Omega}{d\ln r} \right|. \quad (41)$$

Equating the scale height determined by equation (41) with that defined in equation (5) yields a one-to-one correspondence between the gas fraction and the mass accretion rate:

$$f_g = \left(\frac{8}{\alpha Q^2} \left| \frac{d\ln\Omega}{d\ln r} \right|^{-1} \frac{\dot{M}G}{(\Omega r)^3} \right)^{1/3}. \quad (42)$$

Since $\Omega \propto r^{-1}$ in an isothermal potential, equation (42) shows that a constant gas fraction implies a constant accretion rate. On small scales, where the black hole dominates the gravitational potential, $f_g \propto r^{1/2}$ for constant \dot{M} .

In reality, the accretion rate (or f_g) is not constant. As gas accretes from larger to smaller radii and some of the gas is converted into stars to maintain $Q \sim 1$, the accretion rate decreases monotonically. At the outer radius of the disk R_{out} , we assume that gas is supplied at a rate \dot{M}_{out} . At any radius $r < R_{\text{out}}$ the accretion rate $\dot{M}(r)$ is

$$\dot{M}(r) = \dot{M}_{\text{out}} - \int_r^{R_{\text{out}}} 2\pi r' \dot{\Sigma}_* dr'. \quad (43)$$

If the star formation rate required to maintain $Q \sim 1$ is large enough, all of the gas goes into stars and the accretion rate becomes vanishingly small. To quantify this it is useful to consider two timescales characterizing the disk: (1) the advection timescale $\tau_{\text{adv}} = r/V_r$ and (2) the star formation timescale $\tau_* = 1/(\eta\Omega)$. At any radius in the disk, there is a critical accretion rate \dot{M}_c for which $\tau_{\text{adv}} = \tau_*$. Taking the optically-thick limit and assuming $\kappa = \kappa_0 T^2$ (§2.3) yields

$$\dot{M}_c = r^2 \left(\frac{2^{13/2}\pi^3 G Q \sigma_{\text{SB}}}{3\kappa_0^2 \epsilon^2 c^3} \right)^{1/2} \sim 280 r_{200}^2 \epsilon_3^{-1} \kappa_{3.6}^{-1} Q^{1/2} M_\odot \text{yr}^{-1}, \quad (44)$$

where we have scaled the radius to 200 pc in anticipation of numerical calculations described below. If the gas accretion rate in the disk satisfies $\dot{M} > \dot{M}_c$, then $\tau_{\text{adv}} < \tau_*$ and the gas is able to accrete inwards to smaller radii. By contrast if $\dot{M} < \dot{M}_c$, then $\tau_{\text{adv}} > \tau_*$ and most of the gas is converted into stars at radius r without flowing significantly inwards. We note that gas supply rates exceeding \dot{M}_c seem plausible in view of the fact that many ULIRGs have star formation rates greater than \dot{M}_c .

Equation (44) has several important properties. First, \dot{M}_c is seemingly independent of the viscosity. This results from the fact that we have assumed $\kappa \propto T^2$, which is valid only at low temperatures and thus large radii. For general κ or in the optically-thin limit, \dot{M}_c depends explicitly on the viscosity (see Appendix D). Second, \dot{M}_c is an *increasing* function of radius. Thus if gas is supplied at the outer radius R_{out} at a rate $\dot{M}_{\text{out}} > \dot{M}_c$, significant gas accretion can continue to smaller radii. However, on scales smaller than ~ 10 pc, the central disk temperature is high enough that dust sublimates, κ decreases dramatically, and the star formation rate required to maintain $Q \sim 1$ increases (Fig. 2; see also Sirk & Goodman 2003). The

large star formation rate at small radii makes it difficult to fuel a central accretion disk at a rate sufficient to explain bright AGN. This competition between star formation (τ_*) and inflow (τ_{adv}), particularly throughout the opacity gap on 0.1–10 pc scales, determines the rate at which a central AGN is fueled.

3.1. A Model of AGN Fueling

In Appendix C we collect the equations and parameters used in this section to derive the properties of starburst and AGN disks. As in §2, we assume that $\Omega = \Omega_K$, but here we account for the gravitational potential of the black hole: $\Omega_K^2 = GM_{\text{BH}}/r^3 + 2\sigma^2/r^2$. The black hole mass is assumed to be given by the $M_{\text{BH}} - \sigma$ relation: $M_{\text{BH}} \simeq 2 \times 10^8 \sigma_{200}^4 M_\odot$ (Tremaine et al. 2002; Ferrarese & Merritt 2000; Gebhardt et al. 2000). In calculating vertical hydrostatic equilibrium, we include gas pressure, which is important for $r \lesssim 1$ pc. The most important change relative to the model of §2 is the use of a consistent accretion rate that accounts for the loss of gas locally to star formation (eq. [43]).

Although the critical accretion rate \dot{M}_c at which $\tau_{\text{adv}} = \tau_*$ does not depend that strongly on the viscosity in the disk at large radii (eq. [44]), the fate of gas at small radii in the opacity gap is a very strong function of the rate of angular momentum transport. The efficiency of angular momentum transport is important because, for fixed \dot{M} , higher viscosity implies lower surface density and thus self-gravity is comparatively less problematic. Indeed, it is well-known that local angular momentum transport — such as is produced by the magnetorotational instability (Balbus 2003) — is incapable of supplying sufficient gas to a central black hole to account for luminous AGN (e.g., Shlosman & Begelman 1989; Shlosman et al. 1990; Goodman 2003).

One possible solution to this problem is that angular momentum transport proceeds by global torques such as would be provided by stellar bars, spiral waves, or large-scale magnetic stresses (Shlosman et al. 1990; Goodman 2003).¹¹ In this section, we use a phenomenological prescription to describe this process: we assume that the radial transport of gas by a global torque allows the radial velocity to approach a constant fraction m of the local sound speed (Goodman 2003). In this case,

$$\dot{M} = 2\pi r \Sigma_g V_r = \frac{2^{3/2}\Omega^3 r h^2 m}{GQ} \quad (45)$$

and the relationship between accretion rate and gas fraction is given by

$$f_g = \left(\frac{2^{3/2}}{Qm} \frac{\dot{M}G}{(\Omega r)^3} \right)^{1/2} \quad (46)$$

instead of equation (42). Our hope is that, much as the Shakura-Sunyaev prescription provides a useful zeroth-order model for local angular momentum transport in disks, the above model captures some of the essential physics of disks in which angular momentum transport is dominated by global torques. With equation (45) to relate the gas surface density to the gas accretion rate, we solve the equations of Appendix C to determine the structure of the disk.

¹¹ An alternative possibility not considered here is that AGN are fueled by low angular momentum gas (Goodman 2003), including perhaps the hot ISM in clusters of galaxies (e.g., Nulsen & Fabian 2000).

3.2. Results

The dashed lines in Figure 6 show the mass accretion rate \dot{M} as a function of radius for $\dot{M}_{\text{out}} = 80, 160, 220, 320$, and $640 \text{ M}_{\odot} \text{ yr}^{-1}$ in a model with $\sigma = 300 \text{ km s}^{-1}$ ($M_{\text{BH}} \simeq 10^9 \text{ M}_{\odot}$), $R_{\text{out}} = 200 \text{ pc}$, and with dynamical angular momentum transport specified by $m = 0.2$. The black hole dominates the gravitational potential for $r \lesssim 50 \text{ pc}$. The solid lines show the local star formation rate \dot{M}_{\star} defined by $\dot{M}_{\star} = \pi r^2 \dot{\Sigma}_{\star}$.¹²

There are two types of solution represented in Figure 6. The two models with the smallest \dot{M}_{out} lose essentially all of the supplied gas at large radii to star formation. At $r \sim 20 - 40 \text{ pc}$ in these two models the star formation rate becomes so low that \dot{M} approaches a constant near $\sim 0.1 \text{ M}_{\odot} \text{ yr}^{-1}$. This occurs when the central temperature decreases sufficiently that gas pressure dominates. These models have $\tau_{\text{adv}} > \tau_{\star}$ at R_{out} and $\dot{M}_{\text{out}} < \dot{M}_c(R_{\text{out}})$. They are starburst-dominated and the star formation occurs predominantly at $\sim R_{\text{out}}$.

For the three models shown with $\dot{M}_{\text{out}} \geq 220 \text{ M}_{\odot} \text{ yr}^{-1}$ the results are qualitatively different. In these models, \dot{M}_{out} is large enough that star formation persists for more than a decade in radius from $R_{\text{out}} = 200 \text{ pc}$ down to $r \sim 1 - 10 \text{ pc}$. At these small scales, the temperature is sufficiently hot that dust sublimates and the opacity decreases sharply (see Figure 1). Because $\dot{\Sigma}_{\star} \propto \Sigma_g / \kappa$ in the optically-thick limit, the star formation rate must increase dramatically to maintain $Q \sim 1$. The increase in \dot{M}_{\star} as the opacity gap is encountered is typically an order of magnitude. Although these star formation rates are large, they are much smaller than those computed for the constant \dot{M} (or constant f_g) solutions in Figure 2 (§2). In the models with variable f_g , an equilibrium between advection and star formation, expressed by the equality $\tau_{\text{adv}} = \tau_{\star}$, limits the star formation rate in the opacity gap (Appendix A). Each of these high \dot{M}_{out} disk models has a gas accretion rate of $\sim 4 \text{ M}_{\odot} \text{ yr}^{-1}$ at $r \sim 0.01 \text{ pc}$, sufficient to power a luminous AGN. That these models have nearly identical accretion rates at small radii follows from the fact that $\tau_{\text{adv}} = \tau_{\star}$ in the opacity gap. In Appendix A we present an analytical model for the structure of the disk in this region and provide simple formulae for the black hole accretion rate.

As Figure 6 shows, there is a strong bifurcation between models that fuel a central AGN and those that do not. The critical mass supply rate distinguishing these two classes of solutions is close to \dot{M}_c as estimated in equation (44) by equating τ_{adv} and τ_{\star} .

For comparison with these calculations assuming dynamical angular momentum transport, we have also calculated disk solutions employing a local α -viscosity (eq. 41). With $\alpha = 0.3$, the disk structure exterior to the opacity gap is very similar to the models with dynamical angular momentum transport because h/r is large on scales of R_{out} in the models with large \dot{M}_{out} . Therefore, a local viscosity can transport gas from several hundred parsec scales down to $\sim 10 \text{ pc}$ scales in gas-rich starbursts. However, we find that a local viscosity cannot transport

¹² If f_g exceeds unity at R_{out} , then we expect the disk to become globally self-gravitating. Through equation (46), this condition sets a “maximum” mass accretion rate, $\dot{M}_{\text{out}}^{\text{max}} \sim 1250 \sigma_{300}^3 m_{0.2} Q \text{ M}_{\odot} \text{ yr}^{-1}$, above which the approximations of this paper break down. For these reasons, we do not consider models with $\dot{M}_{\text{out}} > 640 \text{ M}_{\odot} \text{ yr}^{-1}$ for the parameters of Figure 6. Equation (5) also shows that as $f_g \rightarrow 1$, $h/r \rightarrow 1$. For models in which h/r or f_g exceeds unity, we expect m or α to increase because of the large gas fraction (as in the “bars within bars” model of Shlosman et al. 1989), a wind to be driven from the disk surface (thereby limiting \dot{M}_{out} dynamically), or perhaps the gas to be pushed out radially (R_{out} increases) to maintain $h/r \sim 1$.

¹³ In these calculations, we have assumed that dynamical angular momentum transport acts throughout the disk. On sub-parsec scales near the black hole, perhaps at R_{AGN} where Q becomes greater than unity, we expect accretion to be driven instead by local viscosity. This will modify the density, scale height, etc., close to the black hole ($\lesssim 0.5 \text{ pc}$ in Figure 7), but will not change our conclusions about the need for angular momentum transport by global torques at larger radii.

gas through the opacity gap at a rate sufficient to fuel bright AGN; typical black hole accretion rates are several orders of magnitude smaller than those with dynamical angular momentum transport (see Appendix A).

In the three models with $\dot{M}_{\text{out}} \geq 220 \text{ M}_{\odot} \text{ yr}^{-1} > \dot{M}_c$, we can distinguish between the outer “starburst disk”, where the heating of the disk is dominated by star formation ($\sigma_{\text{SB}} T_{\text{eff}}^4 = (1/2) \epsilon \dot{\Sigma}_{\star} c^2$), and the inner “AGN disk”, where the heating is dominated by accretion ($\sigma_{\text{SB}} T_{\text{eff}}^4 = (3/8\pi) \dot{M} (1 - \sqrt{R_{\text{in}}/r}) \Omega^2$). The transition between these two regimes occurs at $R_{\text{AGN}} \sim 0.5 \text{ pc}$ in the models presented in Figure 6. At this radius, accretion heating is sufficient to produce $Q > 1$ and star formation ceases.

By combining the equations describing the “starburst” disk at $r > R_{\text{AGN}}$ with those describing the “AGN disk” at $r < R_{\text{AGN}}$ we have computed the full radial structure of models from hundreds of parsecs down to the central black hole. We note again that there are multiple solutions at some radii and that we have selected what we believe is the physical disk solution as described in Appendix B. As an example of the full radial disk structure, Figure 7 shows the results for the model with $\dot{M}_{\text{out}} = 320 \text{ M}_{\odot} \text{ yr}^{-1}$ (see also Fig. 6). In the middle left panel, note that gas pressure dominates radiation pressure over ~ 1 decade in radius inside the opacity gap at $r \lesssim 1 \text{ pc}$ (Appendix A), but that radiation pressure dominates at all other radii.¹³

Assuming that every annulus in the disk radiates as a blackbody and that the disk is viewed face-on, the spectral energy distribution of our disk models can be computed using

$$\lambda L_{\lambda} = \frac{2\pi hc^2}{\lambda^4} \int_{R_{\text{in}}}^{R_{\text{out}}} \frac{2\pi r dr}{\exp[hc/\lambda k_{\text{B}} T_{\text{eff}}(r)] - 1}. \quad (47)$$

The resulting multi-color blackbody spectra for the models presented in Figure 6 are shown in Figure 8, assuming an inner disk radius of $R_{\text{in}} = 3(2GM_{\text{BH}}/c^2)$. The models with small mass supply rate ($\dot{M}_{\text{out}} < \dot{M}_c$) have the lowest bolometric luminosity and virtually all of their flux is generated by the starburst at R_{out} . The spectra of these models peak at $\sim 50 \mu\text{m}$, corresponding to an outer disk dust temperature of $\sim 70 \text{ K}$. For higher \dot{M}_{out} , the dust temperature at R_{out} increases somewhat and the spectral peak moves to shorter wavelengths.

Higher \dot{M}_{out} models have similar FIR spectra. However, at $\sim 8 \mu\text{m}$ they exhibit an additional spectral peak. This peak is produced by the inner ring of star formation on $1 - 10 \text{ pc}$ scales shown in Figure 6, which is caused by the decrease in the opacity of the disk at the dust sublimation temperature, $T_{\text{sub}} \sim 1000 \text{ K}$. Although T_{sub} sets the central temperature of the disk where this sudden increase in $\dot{\Sigma}_{\star}$ occurs, the disk is typically optically thick at these radii and the effective temperature can be a factor of $\sim 3 - 4$ smaller, accounting for the fact that the spectral peak associated with star formation in the opacity gap is at $\sim 8 \mu\text{m}$. Together, the FIR peak from the outer starburst ring and the peak from the inner starburst ring create a broad IR peak spanning ~ 1.5 decades in wavelength.

The distinguishing feature of the models with large \dot{M}_{out} is the significant contribution of the AGN to the bolometric luminosity: the UV emission in Figure 8 is comparable to or dominates the peaks at ~ 8 and ~ 50 μm . Figure 8 suggests that quasar accretion disks can plausibly be fed by radiation pressure supported starburst disks at larger radii. Indeed, the broad but sub-dominant IR peak and the magnitude of the AGN luminosity in our models are reasonably consistent with composite quasar spectra (Elvis et al. 1994; Haas et al. 2003).

It should be noted that the spectra shown in Figure 8 are photospheric and do not include AGN reprocessing. Because the disk may intercept some of the AGN emission, we expect that reprocessing could lead to an additional emission component at $\sim 1-2\mu\text{m}$ if dust in the surface layers of the disk is heated to the sublimation temperature.

3.3. Vertical Structure & Nuclear Obscuration in AGN

At radii ~ 1 pc the models shown in Figure 7 have the interesting property that the central temperature of the disk is above the sublimation temperature of dust while the effective (surface) temperature of the disk is below the sublimation temperature. As a result, there is a large vertical gradient in the opacity of the disk. Because the disk is radiation pressure dominated, this large gradient in the opacity has important implications for the disk's vertical structure. Here we argue that the photosphere of the disk can lie a distance $h_{ph} \sim r$ off of the midplane even though the midplane scale height is small, with $h \ll r$ (where $h = c_s/\Omega$ is evaluated using the midplane properties of the disk). We then discuss the implications of this result.

The equations governing the vertical structure of the disk include those of vertical hydrostatic equilibrium and vertical energy transport:

$$\frac{dp}{dz} = -\rho\Omega^2 z, \quad (48)$$

where $p = p_{\text{gas}} + p_{\text{rad}}$ and we assume that Ω is independent of the height z in the disk. Assuming that energy is transported diffusively by photons implies

$$\frac{dT}{dz} = -\frac{3\kappa\rho F}{16T^3\sigma_{\text{SB}}} \quad (49)$$

where F is the vertical flux of energy. If the disk is radiation pressure dominated, as our models are at most radii, then equations (48) and (49) imply that the flux in the disk must be everywhere equal to the Eddington flux:

$$F = F_{\text{EDD}} = \frac{\Omega^2 cz}{\kappa}. \quad (50)$$

The presence of a large vertical opacity gradient suggests that convection might develop in the outer atmosphere of the disk. However, two arguments show that convection is unlikely to be important in the present context: (1) Our disk models have $\tau_{\text{th}}\Omega \ll 1$, where τ_{th} is the cooling time of the disk (Appendix B). This implies that the diffusion time through the disk is much shorter than the characteristic timescale of buoyant convective motions. In the presence of such strong radiative diffusion, convective modes driven by radiation entropy gradients grow very slowly, if at all (e.g., Blaes & Socrates 2003). (2) Even if convection develops, it is unlikely to carry a significant fraction of the vertical energy flux. Using $F \approx \rho V_c^3$ to estimate the convective velocity V_c required to carry the energy flux we find very

high Mach numbers:

$$\frac{V_c}{c_s} \approx 40M_9^{1/3} \left(\frac{z}{r}\right)^{1/3} \left(\frac{F}{F_{\text{EDD}}}\right)^{1/3} r_{\text{pc}}^{-2/3} T_{1000}^{-2} \kappa_1^{-1/3} \rho_{-15}^{1/6}, \quad (51)$$

where $\rho_{-15} = \rho/10^{-15}$ g cm^{-3} and we have scaled our estimate to parameters appropriate to parsec scale-disks (see Fig. 7). These considerations strongly suggest that radiative diffusion dominates the vertical transport of energy throughout the disk.

Unfortunately, equations (48) and (49) are insufficient to fully specify the vertical structure of the disk. An equation for the vertical generation of energy, dF/dz , is also needed (e.g., Davis et al. 2005). The vertical heating profile is particularly uncertain in the present context where star formation, rather than accretion, dominates the heating of the disk. Given this significant uncertainty, we restrict ourselves to the following simple considerations about the disk's vertical structure.

We assume that the calculations described in the previous sections — that apply to the midplane of the disk — provide an adequate estimate of the star formation rate $\dot{\Sigma}_*$ and, thereby, the flux F required to maintain $Q \sim 1$. This assumes that the atmosphere of the disk does not contribute much flux, a reasonable assumption. Because the disk is radiation pressure dominated near its photosphere, we can estimate the location of the photosphere using $F \approx F_{\text{EDD}}$. This yields

$$h_{ph} \approx \frac{F\kappa_{ph}}{\Omega^2 c} \approx h \left(\frac{\kappa_{ph}}{\kappa_{\text{mid}}}\right), \quad (52)$$

where κ_{ph} is the opacity at the photosphere, evaluated using the effective temperature, and κ_{mid} is the opacity at the midplane, evaluated using the central temperature. Equation (52) shows that if the opacity at the surface of the disk is much larger than the opacity near the midplane, as will inevitably occur in the vicinity of the sublimation temperature of dust, then $h_{ph} \gg h$ and the midplane scale height does not provide a good estimate of the location of the photosphere of the disk.

Figure 9 shows our estimates of the midplane scale-height h/r and the photospheric scale-height h_{ph}/r for models with $\dot{M}_{\text{out}} = 320$ and 640 M_{\odot} yr^{-1} (whose other properties have been described in Figures 6-8). These estimates of the photospheric scale-height show that h_{ph} can readily approach $\sim r$ at $\sim 0.1-10$ pc, even though the midplane scale-height of the disk satisfies $h \ll r$. Because the effective temperature of the disk is $\lesssim T_{\text{sub}}$, the opacity near the photosphere is $\kappa \sim 1$ g cm^{-2} and the hydrogen column through the disk's atmosphere can approach $\sim 10^{24}$ cm^2 . We suggest that this extended dusty atmosphere may account for the presence of obscuring material inferred from observations of AGN (e.g., Antonucci 1993). In particular, although AGN disks are typically classified as being “thin” because $h \ll r$, Figure 9 shows that the photosphere may nonetheless puff up substantially and reach $h_{ph} \sim r$. Some of this material is likely to be unbound and the origin of a dusty outflow.

The disk's extended atmosphere is supported by radiation pressure from a parsec-scale nuclear starburst (in contrast to Pietrini & Krolik 2000, who argued that dusty gas could be supported at $h \sim r$ by radiation pressure from the AGN). Estimating the luminosity of the disk at these radii, $L \equiv \pi r^2 F$, we find

$$L \approx \frac{\pi G M c}{\kappa_{ph}} \left(\frac{h_{ph}}{r}\right) \approx \frac{L_{\text{es}}}{4} \left(\frac{\kappa_{\text{es}}}{\kappa_{ph}}\right) \left(\frac{h_{ph}}{r}\right), \quad (53)$$

where L_{es} is the canonical Eddington luminosity defined using the electron-scattering opacity κ_{es} . Taking $\kappa_{\text{ph}} \sim 10\kappa_{\text{es}}$, equation (53) implies that in order to have $h_{\text{ph}} \sim r$, as suggested by the relative number of Type 1 & Type 2 Seyfert galaxies, the luminosity of the parsec-scale disk must be $\sim 0.01 - 0.1 L_{\text{es}}$. Therefore, in order for the disk to have $h_{\text{ph}} \sim r$, we predict the presence of a very compact nuclear starburst with a luminosity similar to that of the AGN.

Because the luminosity from star formation required to “puff up” the disk is substantial, it is unlikely that this model is relevant to low-luminosity Seyfert 2 galaxies such as NGC 4258 (where there is also strong evidence that the nuclear obscuration is due to a warped disk; e.g., Fruscione et al. 2005). A compact starburst may, however, dynamically support obscuring material in more luminous AGN. In particular, there is evidence for a compact starburst in the prototypical Seyfert 2 Galaxy NGC 1068. IR interferometry of 1068 has also directly resolved warm dusty gas on the parsec scales predicted by our model (Jaffe et al. 2004; Rouan et al. 2004).

4. DISCUSSION & CONCLUSIONS

In standard models of galactic-scale star formation, energy and momentum injected by supernovae and stellar winds are assumed to drive turbulent motions in the interstellar medium of a galaxy (e.g., Silk 1997). This turbulent pressure helps stave off the self-gravity of the disk and maintain marginal stability to gravitational perturbations (Toomre’s $Q \sim 1$). In this paper, we have focused instead on the role of radiation pressure on dust grains in regulating the structure and dynamics of star formation in galaxies. To order of magnitude, the turbulent pressure from supernovae, stellar winds, and the radiation from massive stars are all comparably important when the galactic disk is optically thin to its own IR radiation, as in normal star-forming galaxies. By contrast, when the disk is optically thick to the IR, radiation pressure provides the dominant vertical support against gravity. This condition is met in the inner few hundred parsecs of luminous gas-rich starbursts, most notably in Ultra-luminous Infrared Galaxies (ULIRGs). In addition, the outer parts of accretion disks around AGN are expected to be dominated by radiation pressure on dust. Understanding the dynamics of disks in the radiation pressure dominated limit is therefore crucial for understanding nuclear starbursts and AGN fueling.

We have constructed simple quantitative models of self-regulated disks appropriate to both the optically-thin and optically-thick limits. From these models, we derive the star formation rate per unit area required to maintain $Q \sim 1$. In the optically-thin limit, we find that $\dot{\Sigma}_* \propto \Sigma_g^2$ (eq. [16]), a slightly steep version of the Schmidt law for star formation, whereas in the optically-thick limit, $\dot{\Sigma}_* \propto \Sigma_g^2/\tau_V \propto \Sigma_g/\kappa$ (eq. [28]). Because radiation pressure dominates the vertical pressure support in the optically-thick limit, the star formation rate is sensitive to the opacity (κ), and thus also to the metallicity, of the disk. In fact, each annulus of the disk radiates at its local Eddington limit. This criterion can be written as (see also Scoville 2003) $L/M \sim 10^3 f_{g,0.5} \kappa_1^{-1} L_{\odot}/M_{\odot}$, where the gas fraction f_g is proportional to the disk thickness h/r .

Figure 3 shows that our estimates of the star formation efficiency agree reasonably well with observations, in both starbursts and normal spirals. However, our prediction that the Schmidt law changes in the optically-thick limit (with $\dot{\Sigma}_* \propto$

Σ_g/κ) is difficult to test with current observations and requires further high resolution observations. It is important to stress that in our models the star formation efficiency in the optically-thick nuclei of starbursts is actually *lower* than what would be inferred from an extrapolation of the star formation efficiency in normal star-forming galaxies because of the extra support from radiation pressure in the optically-thick limit (Fig. 3; §2.5).

Our calculations show that in the optically-thick portion of starburst disks near ~ 100 pc, the flux, star formation rate per unit area, and the effective temperature of the disk are roughly constant with characteristic values of $F \sim 10^{13} L_{\odot}$ kpc $^{-2}$, $\dot{\Sigma}_* \sim 10^3 M_{\odot}$ yr $^{-1}$ kpc $^{-2}$, and $T_{\text{eff}} \sim 90$ K (§2.3). To test these predictions, we have estimated the fluxes (temperatures) in the emission regions of ULIRGs using the resolved radio images of Condon et al. (1991) as indicative of the sizes of nuclear starbursts in these systems (the fluxes inferred using FIR blackbody temperatures may not accurately characterize the fluxes in the emission region if there is still significant obscuration at $\gtrsim 20 - 30$ microns). We find excellent agreement with the predictions of our models (Figs. 4 & 5). This supports our interpretation that a significant fraction of the radiation from ULIRGs is produced by an Eddington-limited starburst. In the future, imaging at optically-thin FIR wavelengths will test our assumption that the radio emission traces star formation in ULIRGs.

In our model of starburst disks, the central temperature exceeds the dust sublimation temperature ($T_{\text{sub}} \sim 1000$ K) at radii $\sim 1 - 10$ pc. The opacity of the disk then drops dramatically and the star formation rate required to maintain $Q \sim 1$ is very large (Fig. 2). This poses a severe problem for fueling a central AGN with gas stored in the starburst disk at larger radii (Sirk & Goodman 2003). At first glance it appears that all of the gas is converted into stars in the “opacity gap” with little left available to power a central AGN.

A number of solutions to this problem have been proposed, all of which hinge on the efficiency of angular momentum transport in the disk (Shlosman & Begelman 1989; Goodman 2003). For fixed \dot{M} , higher viscosity implies lower surface density and thus self-gravity is comparatively less problematic. For this reason, we have focused on the possibility that angular momentum transport proceeds via a global torque, as would be provided by a bar, spiral waves, or a large-scale wind. With this prescription for angular momentum transport we have extended our starburst disk models to smaller radii where they connect consistently with AGN disks on sub-parsec scales. A key ingredient to these calculations is an equation that accounts for the radial loss of gas due to star formation (eq. [43]).

Our model provides a way of quantifying the connection between starbursts and AGN activity. In particular, we find two classes of disk models (Figs. 6-8): (1) For mass supply rates at the outer edge of the disk less than a critical rate M_c (eq. [44]), a starburst occurs primarily in a narrow ring at R_{out} . Nearly all of the gas is converted into stars at large radii and the spectrum is dominated by a FIR starburst peak. This class of solutions corresponds to the limit in which the star formation time in the disk is shorter than the viscous time ($\tau_* < \tau_{\text{adv}}$). (2) On the other hand, for $M_{\text{out}} > M_c$, a fraction of the gas accretes inwards to smaller radii because the advection timescale is shorter than the star formation timescale. These disk solutions have an outer starburst at $\sim R_{\text{out}}$ and an inner nuclear starburst ring on $\sim 1 - 10$ pc scales at the opacity gap (Fig. 6). In addition, for fiducial parameters we find that the accretion rate onto the central BH is

$\sim 1 - 10 M_{\odot} \text{ yr}^{-1}$ (Appendix A). Models with $\dot{M}_{\text{out}} > \dot{M}_c$ can be dominated by AGN emission, although there is a prominent contribution in the mid- and far-IR from the inner and outer starbursts (Fig. 8). Both the broad but sub-dominant IR peak and the magnitude of the AGN luminosity in our models are reasonably consistent with composite AGN spectra.

One prediction of our models is that a significant fraction of the IR emission in luminous AGN must be from star formation rather than reprocessing. The star formation is required to support the accretion disk at large radii against its own self-gravity (see Rowan-Robinson 2000 for an observational discussion of this point). We have identified an additional observational consequence of the parsec-scale starburst that is predicted to occur when the temperature of the disk reaches the sublimation temperature of dust. Our estimates suggest that for luminous AGN, the nuclear starburst is able to inflate the photosphere of the disk to a height $h_{ph} \sim r$ (§3.3 and Fig. 9). This extended atmosphere of the disk contains little mass but produces significant obscuration, and may account for some of the nuclear obscuration observed in Type 2 AGN.

As a final application of our calculations, we note that there is direct observational evidence for compact starbursts near massive black holes. In particular, observations of the Galactic Center reveal a population of young O and B stars within the central parsec of our Galaxy. Most of these stars appear to lie in a thin disk located within $0.1 - 0.3$ parsecs of the black hole (Levin & Beloborodov 2003; Genzel et al. 2003). The origin of these stars remains uncertain, but their disk-like kinematics suggests that they might have formed in a dense self-gravitating accretion disk, if the black hole in the Galactic Center were accreting at a much higher rate several million years ago (e.g., Levin & Beloborodov 2003). To explore this hypothesis in the context of our models, Figure 10 shows the star formation rate and accretion rate as a function of radius in models with $\sigma = 75 \text{ km s}^{-1}$, $M_{\text{BH}} = 4 \times 10^6 M_{\odot}$, $R_{\text{out}} = 3 \text{ pc}$, and an α -viscosity with $\alpha = 0.3$ (we also increased the opacity by a factor of three relative to the curves presented in Figure 1 to account for the super-solar metallicity of the Galactic Center). The chosen outer radius is appropriate if the circum-nuclear disk in the Galactic Center — a current reservoir of $\sim 10^4 - 10^5 M_{\odot}$ of gas (e.g., Jackson et al. 1993; Shukla, Yun, & Scoville 2004) — were accreted onto the central black hole. The mass supply rates we have used — $\dot{M}_{\text{out}} = 0.015 - 0.15 M_{\odot} \text{ yr}^{-1}$ — are in the range expected if the circum-nuclear disk were accreted on a viscous timescale $\sim 10^6$ years. Figure 10 shows that the star formation rate in this hypothesized burst of accretion typically has a strong peak at $r \sim 0.1 \text{ pc}$. This is the “inner nuclear starburst” caused by the decrease in opacity when the central disk temperature exceeds the sublimation temperature of dust. The location of this starburst is strikingly similar to the current location of the stellar disk in the Galactic Center.

Several aspects of our calculations require further study. The first is the stability of our disk solutions. It is well known that radiation-pressure supported disks are prone to numerous instabilities: viscous, thermal, convective, and photon-bubble (e.g., Lightman & Eardley 1974; Piran 1978; Blaes & Socrates 2003). Such instabilities have been extensively studied in the context of the central $\sim 10 - 100$ Schwarzschild radii of black hole accretion disks, where the radiation pressure is on free electrons. An important difference between our solutions and these is that

at large radii the disk is heated primarily by star formation, not accretion. We find that as a result, the disk is globally thermally and viscously stable (Appendix B). As in the local ISM, however, the disk may fragment into a multi-phase medium. A second aspect of our model that requires further study is the physics of star formation under the unusual conditions appropriate to gravitationally unstable accretion disks, particularly at radii $\sim \text{pc}$ where the gas is much denser and hotter than in normal star-forming regions. Because $Q \ll 1$ in the absence of star formation, and because the cooling time of the disk is much shorter than the orbital time (Appendix B), we believe that fragmentation of the disk is inevitable. But beyond this, the properties of star formation under these conditions are poorly understood (Goodman & Tan 2004 argued that the disk will form supermassive stars). Another component of our model requiring further study is the interaction of the AGN emission with the flared starburst disk and the tenuous dusty obscuring atmosphere predicted in §3.3.

Finally, we note that large-scale outflows of cold dusty gas are commonly observed from starbursting galaxies, including ULIRGs (Alton et al. 1999; Heckman et al. 2000; Martin 2004). We have recently proposed that radiation pressure on dust is an important mechanism in driving such winds (Murray, Quataert, & Thompson 2005 [MQT]). The disk models presented here provide support for this idea because it is natural to suspect that a radiation pressure supported starburst disk will drive a wind from its photosphere, much as near-Eddington stars drive strong outflows. In MQT we further argued that both starbursts and AGN have a maximum Eddington-like luminosity given by $L_M = 4f_g \sigma^4 c/G$.¹⁴ One can show that the disk models presented in this paper have luminosities $\lesssim L_M$, with the equality obtained (approximately) when $h \sim r$ and the spherical limit employed in MQT is realized. We also note that the results in this paper, together with those of MQT, imply that fueling a luminous AGN requires an accretion rate in the range $\dot{M}_c \lesssim \dot{M}_{\text{out}} \lesssim \dot{M}_{\text{max}} \equiv L_M/(\epsilon c^2)$. With the black hole accretion rate given by equation (A4), this yields a ratio of star formation rate to black hole accretion rate of $\sim 100 - 1000$, similar to the observed ratio of stellar mass to BH mass in nearby galaxies (Magorrian et al. 1998; Häring & Rix 2004).

We thank Reinhard Genzel and Chris McKee for a number of stimulating conversations and for a critical reading of the text. We also thank Omer Blaes, Shane Davis, Bruce Draine, Jeremy Goodman, James Graham, Yoram Lithwick, and Linda Taconni for useful discussions, and Semenov et al. for making their dust opacities publicly available. T.A.T. is supported by NASA through Hubble Fellowship grant #HST-HF-01157.01-A awarded by the Space Telescope Science Institute, which is operated by the Association of Universities for Research in Astronomy, Inc., for NASA, under contract NAS 5-26555. E.Q. is supported in part by NSF grant AST 0206006, NASA grant NAG5-12043, an Alfred P. Sloan Fellowship, and the David and Lucile Packard Foundation. N.M. thanks the Miller Foundation for supporting his stay at UC Berkeley. N.M. is also supported in part by a Canadian Research Chair in Astrophysics.

¹⁴ The “M” in L_M stands for “momentum-driven”.

REFERENCES

Alton, P. B., Davies, J. I., & Bianchi, S. 1999, *A&A*, 343, 51

Antonucci, R. 1993, *ARA&A*, 31, 473

Balbus, S. A. 2003, *ARA&A*, 41, 555

Bell, K. R., & Lin, D. N. C. 1994, *ApJ*, 427, 987

Binney, J., & Tremaine, S., *Galactic Dynamics* (Princeton University Press, Princeton, 1987)

Binney, J., & Merrifield, M., *Galactic Astronomy* (Princeton University Press, Princeton, 1998)

Blaes, O., & Socrates, A. 2003, *ApJ*, 596, 509

Boulares, A., & Cox, D. P. 1990, *ApJ*, 365, 544

Chapman, S. C., Smail, I., Windhorst, R., Muxlow, T., Ivison, R. J., 2004, *ApJ*, 611, 732

Chevalier, R. A. 1974, *ApJ*, 188, 501

Cioffi, D. F., McKee, C. F., & Bertschinger, E. 1988, *ApJ*, 334, 252

Condon, J. J., Huang, Z.-P., Yin, Q. F., & Thuan, T. X. 1991, *ApJ*, 378, 65

Cox, D. P. 1972, *ApJ*, 178, 159

Davis, S., Blaes, O., Hubeny, I., & Turner, N. 2004, submitted to *ApJ*, astro-ph/0408590

Downes, D., Solomon, P. M., & Radford, S. J. E. 1993, *ApJ*, 414, L13

Downes, D., & Solomon, P. M. 1998, *ApJ*, 507, 615

Efstathiou, G. 2000, *MNRAS*, 317, 697

Elmegreen, B. G. 1997, *ApJ*, 477, 196

Elvis, M., et al. 1994, *ApJS*, 95, 1

Ferrarese, L., & Merritt, D. 2000, *ApJ*, 539, L9

Fruscione, A., Greenhill, L., Filippenko, A., Moran, J., Herrnstein, J., Galle, E. 2005, accepted to *ApJ*, astro-ph/0501105

Gammie, C. F. 2001, *ApJ*, 553, 174

Gao, Y., & Solomon, P. M. 2004, *ApJ*, 606, 271

Gebhardt, K., et al. 2000, *ApJ*, 539, L13

Genzel, R., & Cesarsky, C. J. 2000, *ARA&A*, 38, 761

Genzel, R., Tacconi, L. J., Rigopoulou, D., Lutz, D., & Tecza, M. 2001, *ApJ*, 563, 527

Genzel, R., Baker, A. J., Tacconi, L. J., Lutz, D., Cox, P., Guilloteau, S., & Omont, A. 2003, *ApJ*, 584, 633

Goodman, J. 2003, *MNRAS*, 339, 937

Goodman, J., & Tan, J. C., 2004, *ApJ*, 608, 108

Graham, J. R., Carico, D. P., Matthews, K., Neugebauer, G., Soifer, B. T., & Wilson, T. D. 1990, *ApJ*, 354, L5

Haas, M., et al. 2003, *A&A*, 402, 87

Häring, N., & Rix, H. 2004, *ApJ*, 604, L89

Heckman, T. M., Lehnert, M. D., Strickland, D. K., & Armus, L. 2000, *ApJS*, 129, 493

Iwasawa, K., Matt, G., Guainazzi, M., & Fabian, A. C. 2001, *MNRAS*, 326, 894

Jackson, J. M., Geis, N., Genzel, R., Harris, A. I., Madden, S., Poglitsch, A., Stacey, G. J., & Townes, C. H. 1993, *ApJ*, 402, 173

Jaffe, W., et al. 2004, *Nature*, 429, 47

Kennicutt, R. C. 1998, *ApJ*, 498, 541

Kolykhalov, P. I., & Sunyaev, R. A. 1980, *SvAL*, 6, 357

Leitherer, C., et al. 1999, *ApJS*, 123, 3

Levin, Y., & Beloborodov, A. M. 2003, *ApJL*, 590, L33

Levin, Y. 2005, submitted to *MNRAS*, astro-ph/0307084

Lightman, A. P., & Eardley, D. M. 1974, *ApJ*, 187, L1

Magorrian, J., et al. 1998, *AJ*, 115, 2285

Martin, C. L., & Kennicutt, R. C. 2001, *ApJ*, 555, 301

Martin, C. L. 2004, submitted to *ApJ*, Astro-Ph/0410247

McKee, C. F., & Ostriker, J. P. 1977, *ApJ*, 218, 148

Meurer, G. R., Heckman, T. M., Lehnert, M. D., Leitherer, C., & Lowenthal, J. 1997, *AJ*, 114, 54

Mihos, J. C., & Hernquist, L. 1996, *ApJ*, 464, 641

Murray, N., Quataert, E., & Thompson, T. A. 2005, *ApJ*, 618, 569

Navarro, J. F., Frenk, C. S., & White, S. D. M. 1997, *ApJ*, 490, 493

Nulsen, P. E. J., & Fabian, A. C. 2000, *MNRAS*, 311, 346

Paczynski, B. 1978, *Acta Astronomica*, 28, 91

Pietrinini, P., & Krolik, J. H. 2000, *ApJ*, 539, 216

Piran, T. 1978, *ApJ*, 221, 652

Pollack, J. B., McKay, C. P., & Christofferson, B. M. 1985, *Icarus*, 64, 471

Rouan, D., et al. 2004, *A&A*, 417, L1

Rowan-Robinson, M. 2000, *MNRAS*, 316, 885

Sakamoto, K., Scoville, N. Z., Yun, M. S., Crosas, M., Genzel, R., & Tacconi, L. J. 1999, *ApJ*, 514, 68

Scoville, N. Z., Polletta, M., Ewald, S., Stolovy, S. R., Thompson, R., & Rieke, M. 2001, *ApJ*, 122, 3017

Scoville, N. Z. 2003, *JKAS*, 36, 167

Semenov, D., Henning, T., Helling, C., Ilgner, M., & Sedlmayr, E. 2003, *A&A*, 410, 611

Shlosman, I., & Begelman, M. C. 1989, *ApJ*, 341, 685

Shlosman, I., Begelman, M. C., & Frank, J. 1990, *Nature*, 345, 679

Shukla, H., Yun, M. S., & Scoville, N. Z. 2004, *ApJ*, 616, 231

Silk, J. 1997, *ApJ*, 481, 703

Sirko, E., & Goodman, J. 2003, *MNRAS*, 341, 501

Smith, H. E., Lonsdale, C. J., Lonsdale, C. J., & Diamond, P. J. 1998, *ApJ*, 493, L17

Sodroski, T. J., Odegard, N., Arendt, R. G., Dwek, E., Weiland, J. L., Hauser, M. G., & Kelsall, T. 1997, *ApJ*, 480, 173

Soifer, B. T., et al. 2000, *AJ*, 119, 509

Soifer, B. T., Neugebauer, G., Matthews, K., Becklin, E. E., Ressler, M., Werner, M. W., Weinberger, A. J., & Egami, E. 1999, *ApJ*, 513, 207

Solomon, P. M., Downes, D., Radford, S. J. E., & Barrett, J. W. 1997, *ApJ*, 478, 144

Tacconi, L., et al. 2005, in preparation for *ApJ*

Thornton, K., Gaudlitz, M., Janka, H.-T., & Steinmetz, M. 1998, *ApJ*, 500, 95

Toomre, A. 1964, *ApJ*, 139, 1217

Tremaine, S., et al. 2002, *ApJ*, 574, 740

Wolfire, M. G., Hollenbach, D., McKee, C. F., Tielens, A. G. G. M., & Bakes, E. L. O. 1995, *ApJ*, 443, 152

Yun, M. S., & Carilli, C. L. 2002, *ApJ*, 568, 88

APPENDIX

APPENDIX A: THE BLACK HOLE ACCRETION RATE

An interesting feature of the results shown in Figure 6 is that all of the models with $\dot{M}_{\text{out}} > \dot{M}_c$ deliver precisely the same amount of mass to the AGN disk at small radii. More specifically, all of the dashed lines for $\dot{M}_{\text{out}} \geq 220 \text{ M}_\odot \text{ yr}^{-1}$ in Figure 6 come together and attach to a single power-law solution in the opacity gap between $r \sim 1 - 10 \text{ pc}$, and then settle onto a constant $\dot{M} \approx 4 \text{ M}_\odot \text{ yr}^{-1}$ solution at smaller radii. In this appendix we explain why this is the case.

The steep drop in the opacity in Figure 1 occurs when the central disk temperature reaches the sublimation temperature T_{sub} at a radius R_{sub} . In the models presented in Figure 6 with $\dot{M} > \dot{M}_c$, R_{sub} corresponds to the sudden increase in \dot{M}_* between ~ 1 and $\sim 10 \text{ pc}$. The rapid decrease in κ inside the opacity gap can be approximated by a power law, $\kappa(T \gtrsim T_{\text{sub}}) = \kappa_{\text{sub}} T^\beta$. For example, in the opacity models of Bell & Lin (1994), $\beta = -24$ and $T_{\text{sub}} \sim 900 \text{ K}$ (see Fig. 1). Because the star formation rate required to maintain $Q \sim 1$ in the optically-thick limit is given by $\dot{\Sigma}_* \propto \Sigma_g / \kappa$ (eq. [28]), one might expect $\dot{\Sigma}_*$ to increase by ~ 5 orders of magnitude inside the opacity gap because κ decreases by this amount at T_{sub} (see Fig. 1). In the models with constant f_g shown in Figure 2, this is precisely what happens. However, when we self-consistently solve for $\dot{M}(r)$ (eq. [43]), as in the models presented in Figure 6, the results are qualitatively different. The star formation rate increases by only ~ 1 order of magnitude at $r \sim R_{\text{sub}}$ because of an important physical effect. As κ decreases and \dot{M}_* increases, the accretion rate must decrease because the gas is depleted as a result of star formation. This leads to a lower surface density and, therefore, a lower star formation rate is required to maintain $Q \sim 1$. Thus, an equilibrium is established between star formation and advection in the opacity gap ($\tau_{\text{adv}} = \tau_*$). An analytic solution representing this balance between star formation and accretion can be derived by solving equation (43) for $\dot{M}(r)$ using $\kappa \propto T^\beta$, $T \propto \Sigma_g^{1/2}$ (eq. [26]), $\dot{\Sigma}_* \propto \Sigma_g / \kappa$ (eq. [28]), and the fact that there is a one-to-one relationship between f_g and \dot{M} . If angular momentum transport proceeds via global torques, the $f_g - \dot{M}$ relation is given by equation (46), and the analytic solution for $\dot{M}(r)$ takes the form

$$\dot{M}(r)^{1/2+\beta/4} - \dot{M}(R_{\text{sub}})^{1/2+\beta/4} = A \left(r^{3/4+5\beta/8} - R_{\text{sub}}^{3/4+5\beta/8} \right), \quad (\text{A1})$$

where A is a β -dependent constant that will be specified below. Because β is $\ll 0$ in the opacity gap, the solution quickly loses memory of the initial conditions at R_{sub} . As a result, a single universal equilibrium power law solution for $\dot{M} \approx \dot{M}_*$ exists in the opacity gap. Because of this equilibrium between star formation and advection, the increase in \dot{M}_* at R_{sub} is much less pronounced in these solutions than in the constant f_g models (compare Fig. 2 & 6).

The general expression for the constant A for arbitrary β is a bit awkward, but the limit $\beta \rightarrow -\infty$ (as appropriate for a step function in opacity) provides a useful approximation. In this limit, the accretion rate inside the opacity gap is given by

$$\dot{M}(r) \approx \frac{4\sigma_{\text{SB}}}{3c} T_{\text{sub}}^4 \frac{4m\pi r}{\Omega} \approx 720 T_{1000}^4 m_{0.1} r_{10}^{5/2} M_9^{-1/2} \text{ M}_\odot \text{ yr}^{-1}, \quad (\text{A2})$$

where $T_{1000} = T_{\text{sub}}/1000 \text{ K}$, $m_{0.1} = m/0.1$, $r_{10} = r/10 \text{ pc}$, and $M_9 = M_{\text{BH}}/10^9 \text{ M}_\odot$. Note that the normalization of \dot{M} in equation (A2) depends only on the black hole mass M_{BH} , the Mach number $m = V_r/c_s$, and the dust opacity law through T_{sub} . This explains why all of the solutions with $\dot{M}_{\text{out}} > \dot{M}_c$ in Figure 6 are the same inside the opacity gap. Note also that because $\dot{M}(r)$ is a power-law inside the opacity gap, the star formation rate $\dot{M}_*(r)$ is as well (see eq. [43]). Indeed, for these solutions, $\dot{M}_*(r) \equiv \pi r^2 \dot{\Sigma}_* = (5/4) \dot{M}(r)$, in good agreement with Figure 6. Finally, because $\dot{M}_* \propto r^{5/2}$ in the opacity gap, both T_{eff}^4 and $\dot{\Sigma}_*$ are proportional to $r^{1/2}$. The central temperature T and the surface density Σ_g , on the other hand, are independent of radius.

As is clear from Figure 6, the equilibrium power law solution for \dot{M} given in equation (A2) does not persist to arbitrarily small radii. Because ρ increases and T is constant in the opacity gap, gas pressure eventually dominates radiation pressure. The two pressures are comparable at a radius R_{EOS} given by

$$R_{\text{EOS}} \sim 1 M_9^{5/9} \dot{M}_1^{-2/3} m_{0.1}^{2/3} Q^{-8/9} \text{ pc}, \quad (\text{A3})$$

where $\dot{M}_1 = \dot{M}/1 \text{ M}_\odot \text{ yr}^{-1}$. For $r < R_{\text{EOS}}$, one can show that star formation is no longer a significant impediment to accretion: \dot{M}_* drops precipitously and \dot{M} approaches a constant. As a result, we can estimate the accretion rate onto the black hole by evaluating equation (A2) at $r \sim R_{\text{EOS}}$. This yields

$$\dot{M}_{\text{BH}} = 2^{9/4} T_{\text{sub}}^{3/2} m M_{\text{BH}}^{1/3} G^{-1/2} \left(\frac{\sigma_{\text{SB}} \pi}{3c} \right)^{1/6} \left(\frac{k_{\text{B}}}{Q m_p} \right)^{5/6} \sim 2 T_{1000}^{3/2} m_{0.1} M_9^{1/3} Q^{-5/6} \text{ M}_\odot \text{ yr}^{-1}, \quad (\text{A4})$$

where we emphasize that m is the Mach number in the opacity gap region; even if angular momentum transport becomes inefficient for $r < R_{\text{EOS}}$ (e.g. $m \ll 0.1$ or a transition to local viscosity with $\alpha \lesssim 0.1$ occurs), \dot{M}_{BH} remains unchanged. Using equation (A4) and taking $L_{\text{BH}} = \zeta \dot{M}_{\text{BH}} c^2$ we find that

$$L_{\text{BH}} \sim 10^{46} \zeta_{0.1} T_{1000}^{3/2} m_{0.1} M_9^{1/3} Q^{-5/6} \text{ ergs s}^{-1}, \quad (\text{A5})$$

where $\zeta_{0.1} = \zeta/0.1$. This result is in excellent agreement with the models presented in Figures 6 and 8. With $L_{\text{EDD}} = \zeta \dot{M}_{\text{EDD}} c^2 = 4\pi G M_{\text{BH}} c / \kappa_{\text{es}}$, where κ_{es} is the electron scattering opacity, we find that $\dot{M}_{\text{BH}} / \dot{M}_{\text{EDD}} \sim 0.1 m_{0.1} \zeta_{0.1} M_9^{-2/3}$. Therefore, for typical parameters, the black hole is fed at a reasonable fraction of its Eddington rate. Because of the scaling with M_{BH} we expect black holes of smaller mass to be preferentially super-Eddington.

Note again that from equation (A4), the accretion rate through the opacity gap into the AGN disk depends primarily on the dust sublimation temperature and on the rate of angular momentum transport in the opacity gap (via the Mach number m). Because of the latter dependence, it is of interest to compare the above expressions with the analogous results assuming that angular momentum transport in the opacity gap is via a local viscosity, for which the $f_g - \dot{M}$ relation is given by equation (42). In this case the accretion rate in the opacity gap is given by

$$\dot{M}(r) = \frac{3\sqrt{2}\alpha}{GQ} \left(\frac{4\sigma_{\text{SB}}}{3c} T_{\text{sub}}^4 \sqrt{2\pi} GQ \right)^{3/2} \frac{1}{\Omega^3} \approx 210\alpha_{0.1} T_{1000}^6 Q^{1/2} M_9^{-3/2} r_{10}^{9/2} M_{\odot} \text{yr}^{-1}, \quad (\text{A6})$$

and the accretion rate onto the black hole is given by

$$\dot{M}_{\text{BH}} = \frac{3\sqrt{2}\alpha}{GQ} \left(\frac{k_{\text{B}} T_{\text{sub}}}{m_p} \right)^{3/2} \approx 2 \times 10^{-3} \alpha_{0.1} Q^{-1} T_{1000}^{3/2} M_{\odot} \text{yr}^{-1}. \quad (\text{A7})$$

Equations (A6) and (A7) highlight the fact that in our models, local viscosity is insufficient to transport matter through the opacity gap at a rate capable of fueling a bright AGN. In practice, we find that equation (A7) sometimes over-estimates the black hole accretion rate relative to our numerical calculations. Although it accurately predicts \dot{M}_{BH} when α is very large (~ 1), for $\alpha \sim 0.1$ the accretion rate is approximately two orders of magnitude smaller than that implied by equation (A7). The explanation is as follows. For models with α -viscosity, in the opacity gap region $\kappa \propto r^{-5/2}$. That is, although κ decreases significantly at R_{sub} , once $\tau_{\text{adv}} = \tau_{\star}$ the opacity increases for $r < R_{\text{sub}}$. If the opacity gets too large then the power law solutions presented here break down because β is no longer large and negative. Because of this, the equilibrium between τ_{adv} and τ_{\star} is broken and as a consequence \dot{M} decreases sharply as star formation consumes the gas supply. Because the star formation rate decreases as the gas supply dwindles, the temperature decreases. The density, however, under our assumption that $Q \sim 1$, continues to increase and thus eventually gas pressure dominates radiation pressure and we encounter a different R_{EOS} . At this point, gas pressure is sufficient to maintain the stability of the disk, $\dot{\Sigma}_{\star}$ becomes very small, and \dot{M} asymptotes at a value significantly less than that implied by equation (A7).

APPENDIX B: DISK STABILITY

Appendix C lists the full set equations we solve for calculating the disk models presented in this paper. Because of the complicated temperature dependence of the opacity (Fig. 1), together with equations (C3) and (C5), we find multiple solutions at some radii. These solutions have the same pressure (by eq. [C3]), but different temperatures and opacities. In order to determine whether all of these solutions are physical, we assess the thermal and viscous stability of our disk solutions in this Appendix. A second motivation for doing so is that radiation pressure dominated disks close to black holes are known to be thermally and viscously unstable in certain circumstances (e.g., Piran 1978), and so it is important to check whether the same is true for our solutions.

B.1 Timescales

There are four relevant timescales characterizing the disk: (1) the dynamical timescale, $\tau_{\text{dyn}} \sim \Omega^{-1}$, (2) the advection timescale, $\tau_{\text{adv}} = r/V_r$, (3) the star formation timescale, $\tau_{\star} = (\eta\Omega)^{-1}$, and (4) the thermal or cooling timescale, $\tau_{\text{th}} = \Sigma_g c_s^2 / F$, where F is the flux. The latter is also the photon diffusion time across the disk.

In the optically-thick limit, and assuming that radiation pressure dominates gas pressure ($p_{\text{rad}}/p_{\text{gas}} \gg 1$), the ratio of the cooling timescale to the dynamical timescale is very small:

$$\frac{\tau_{\text{th}}}{\tau_{\text{dyn}}} \sim \left(\frac{c_s}{c} \right) \tau_{\text{V}}. \quad (\text{B1})$$

For the disk solutions presented in Figure 6, the optical depth is always greater than unity, but not larger than ~ 1000 , even for $r \sim 1$ pc. Typically, the optical depth is closer to ~ 10 –100. This, together with the fact that $c_s \sim f_g \sigma$ (eq. [6]) implies that $\tau_{\text{th}}/\tau_{\text{dyn}} \ll 1$. This is an important difference relative to canonical accretion disk models. For a local α viscosity an accretion-heated disk has $\tau_{\text{th}} \sim \alpha^{-1} \tau_{\text{dyn}} \gg \tau_{\text{dyn}}$.

We may also compare the star formation timescale with the dynamical timescale. Again assuming that $p_{\text{rad}}/p_{\text{gas}} \gg 1$ and that $\tau_{\text{V}} > 1$, we find that

$$\frac{\tau_{\star}}{\tau_{\text{dyn}}} \sim \left(\frac{c}{c_s} \right) \epsilon \tau_{\text{V}}. \quad (\text{B2})$$

As a consequence, throughout our disk models $\tau_{\star}/\tau_{\text{dyn}} > 1$. This result is, of course, in keeping with our assumption that star formation occurs on a timescale longer than the local free-fall timescale (that is, $\eta \leq 1$).

Lastly, we compare the advection timescale with the dynamical timescale. If angular momentum transport is produced by a global torque (as in Figure 6), $\tau_{\text{adv}} \sim \tau_{\text{dyn}}(r/h)m^{-1}$, which is always greater than unity. If angular momentum transport is instead driven by local viscosity, $(\tau_{\text{adv}}/\tau_{\text{dyn}}) \sim (r/h)^2 \alpha^{-1}$. As discussed in §3, the advection timescale can be larger or smaller than the star formation timescale, depending on the ratio of \dot{M} to \dot{M}_c .

These considerations lead to the following well-defined hierarchy of timescales in $Q \sim 1$ disks:

$$\tau_{\text{th}} \ll \tau_{\text{dyn}} \ll \tau_{\star}. \quad (\text{B3})$$

B.2 Thermal Stability

The fact that τ_{th} is much less than τ_{dyn} has important implications for the thermal stability of the disk. In particular, because of this disparity of timescales, the star formation rate per unit area $\dot{\Sigma}_*$ is constant on a timescale τ_{th} . This implies that the volumetric heating rate $q^+ \sim F/h \propto \dot{\Sigma}_*/h$ is a constant on τ_{th} , and, hence, $d \ln q^+ / d \ln T = 0$. However, the volumetric cooling rate in the optically thick limit is $q^- \sim \sigma_{\text{SB}} T^4 / (\tau_{\text{V}} h)$. Taking $\kappa \propto T^\beta$, $d \ln q^+ / d \ln T \propto (4 - \beta)$. Therefore, if $\beta > 4$, the solution is thermally unstable. This condition is only obtained when $\kappa \propto T^{10}$ at $T \sim 2000$ K (see Figure 1; Bell & Lin 1994). All other solutions are thermally stable. In particular, our $Q \sim 1$ radiation-pressure supported starburst disk with $T \sim 100$ K is globally thermally stable, in contrast to radiation-pressure supported disks heated by accretion energy.

In the optically thin limit, the cooling rate is $q^- \sim j \sim \kappa B \propto T^{4+\beta}$, where j is the emissivity. Therefore, if $\beta < -4$, the solution is unstable. There are only two regions where such a condition might obtain and they correspond to sudden decreases in opacity (nearly step functions in $\kappa[T]$) at $T \sim 100 - 200$ K and in the opacity gap at $T \sim 1000$ K in Figure 1. Otherwise, all optically-thin solutions are globally thermally stable.

B.3 Viscous Stability

To evaluate the viscous stability of our disks we must compute the partial derivative $\partial \dot{M} / \partial \Sigma_g$ (e.g., Lightman & Eardley 1974). For $\partial \dot{M} / \partial \Sigma_g < 0$, the disk is viscously unstable and we expect perturbations to grow and disrupt the disk on a timescale τ_{adv} . If angular momentum transport is driven by global torques, $\dot{M} \propto \Sigma_g c_s$. But as a consequence of our assumption of marginal stability against self-gravity ($Q \sim 1$), at any radius, $c_s \propto f_g \propto \dot{M}^{1/2}$. Moreover, because $\tau_{\text{adv}} \gg \tau_{\text{dyn}}$ it is reasonable to maintain $Q \sim 1$ during perturbations to the surface density. These results imply that $\partial \dot{M} / \partial \Sigma_g$ is always greater than zero and the disk is viscously stable. A similar argument applies if angular momentum transport is instead driven by local viscosity ($\dot{M} \propto \Sigma_g c_s^2$). $Q \sim 1$ disks thus appear to be viscously stable.

B.4 Physical Disk Solutions

In the region where $Q \sim 1$, we often find three solutions to our disk equations, one low-temperature optically-thick solution and two high-temperature optically-thin solutions (see also Sirk & Goodman 2003). Throughout this paper we have focused on the low-temperature optically-thick solution as the physical solution. Here we justify this choice.

All three of the disk solutions appear viscously stable. The two high-temperature solutions bracket the opacity gap: one has $T = T_{\text{sub}} \sim 1000$ K and the other occurs at $T \sim 2000 - 5000$ K. By the optically-thin thermal stability criteria of §B.2, the solution with $T \sim 1000$ K is thermally unstable because β is very large and negative. This solution is therefore probably unphysical. The solution with $T \sim 2000 - 5000$ K is formally thermally stable because β is positive (Fig. 1). However, the opacity curve employed here does not take into account important line cooling processes in this temperature range. Indeed, studies of the ISM have shown that gas with $T \sim 2000 - 5000$ K is thermally unstable (Wolfire et al. 1995). Although the ISM of dense starburst nuclei may be interestingly different than of normal star-forming galaxies, it is still likely that optically thin gas at several thousand Kelvin gas is thermally unstable. For this reason we do not believe that the $T \sim 2000 - 5000$ K solution represents a physical global equilibrium of the disk. It is, however, likely that the existence of multiple solutions at the same pressure implies that the ISM is prone to breaking up into a multi-phase medium. A detailed investigation of the multi-phase structure of the ISM in starburst galaxies is clearly of interest, but beyond the scope of this paper.

APPENDIX C: DISK EQUATIONS

The equations employed in constructing the models shown in Figures 6-8 and described in §3 are

$$\Omega(r) = \Omega_K(r) = \left(\frac{GM_{\text{BH}}}{r^3} + \frac{2\sigma^2}{r^2} \right)^{1/2} \quad (\text{C1})$$

$$\dot{\Sigma}_* = \Sigma_g \Omega \eta \quad (\text{C2})$$

$$p_{\text{gas}} + \epsilon \dot{\Sigma}_* c \left(\frac{1}{2} \tau_{\text{V}} + \xi \right) = \rho h^2 \Omega^2 \quad (\text{C3})$$

$$p_{\text{gas}} = \rho k_{\text{B}} T / m_p \quad (\text{C4})$$

$$T^4 = \frac{3}{4} T_{\text{eff}}^4 \left(\tau_{\text{V}} + \frac{2}{3\tau_{\text{V}}} + \frac{4}{3} \right) \quad (\text{C5})$$

$$\tau_{\text{V}} = \kappa \Sigma_g / 2 \quad (\text{C6})$$

$$\Sigma_g = 2\rho h \quad (\text{C7})$$

$$\dot{M} = 4\pi Rh\rho V_r = 4\pi Rh\rho m c_s = 4\pi Rh^2 \rho \Omega m \quad (\text{C8})$$

$$\dot{M} = \dot{M}_{\text{out}} - \int_{R_{\text{out}}}^r 2\pi r \dot{\Sigma}_* dr \quad (\text{C9})$$

In the outer part of the disk where accretion heating is insufficient to maintain $Q \sim 1$, these equations are solved subject to the conditions

$$\rho = \frac{\Omega^2}{\sqrt{2}\pi GQ} \quad (\text{C10})$$

(with $Q = 1$) and

$$\sigma_{\text{SB}} T_{\text{eff}}^4 = \frac{1}{2} \epsilon \dot{\Sigma}_* c^2 + \frac{3}{8\pi} \dot{M} \left(1 - \sqrt{R_{\text{in}}/r} \right) \Omega^2. \quad (\text{C11})$$

In the inner part of the disk where accretion heating maintains $Q > 1$, equations (C10) and (C11) are replaced by

$$\sigma_{\text{SB}} T_{\text{eff}}^4 = \frac{3}{8\pi} \dot{M} \left(1 - \sqrt{R_{\text{in}}/r} \right) \Omega^2. \quad (\text{C12})$$

The radius at which $Q > 1$ is denoted R_{AGN} . Throughout this work we set $\xi = 1$ in equation (C3) and $\epsilon = 10^{-3}$ in equation (C11). M_{BH} is specified by $M_{\text{BH}} = 2 \times 10^8 \sigma_{200}^4 M_{\odot}$. The inner edge of the AGN disk is taken to be at $R_{\text{in}} = 3(2GM_{\text{BH}})/c^2$. \dot{M}_{out} and R_{out} are the mass supply rate at the outer boundary and the location of the outer boundary, respectively. In equation (C8), we generally take $m = 0.1 - 0.2$.

When calculating disks whose accretion is driven by a local viscosity, as in Figure 10, we replace equation (C8) with

$$\dot{M} = 2\pi\nu\Sigma_g \left| \frac{d \ln \Omega}{d \ln r} \right| = \frac{2^{3/2} \alpha h^3 \Omega^3}{GQ} \left| \frac{d \ln \Omega}{d \ln r} \right|. \quad (\text{C13})$$

APPENDIX D: THE CRITICAL MASS SUPPLY RATE

As shown in Figure 6 and Appendix A, when \dot{M}_{out} exceeds a critical rate \dot{M}_c , gas can accrete to small radii fueling a bright AGN. By contrast, for $\dot{M}_{\text{out}} < \dot{M}_c$, star formation consumes the gas in a narrow range of radii at $\sim R_{\text{out}}$. In the optically-thick limit, and to the extent that κ may be approximated by $\kappa_0 T^2$, the critical mass supply rate is given in equation (44).

The balance between star formation and accretion is different in the optically-thin limit than it is in the optically-thick limit. To show this, we note that equation (43) admits a simple power-law solution when angular momentum transport is driven by a global torque (eq. [45]):

$$\dot{M}(r) \propto r^{\sigma/(\sqrt{2}\epsilon\xi cm)}. \quad (\text{D1})$$

Because

$$\frac{\sigma}{\sqrt{2}\epsilon\xi cm} \sim 7\sigma_{300}(\epsilon_3 \xi m_{0.1})^{-1} \quad (\text{D2})$$

we see that unless there is a very efficient global torque ($m \gtrsim 1$), gas will be converted into stars rather than accreting to smaller radii.

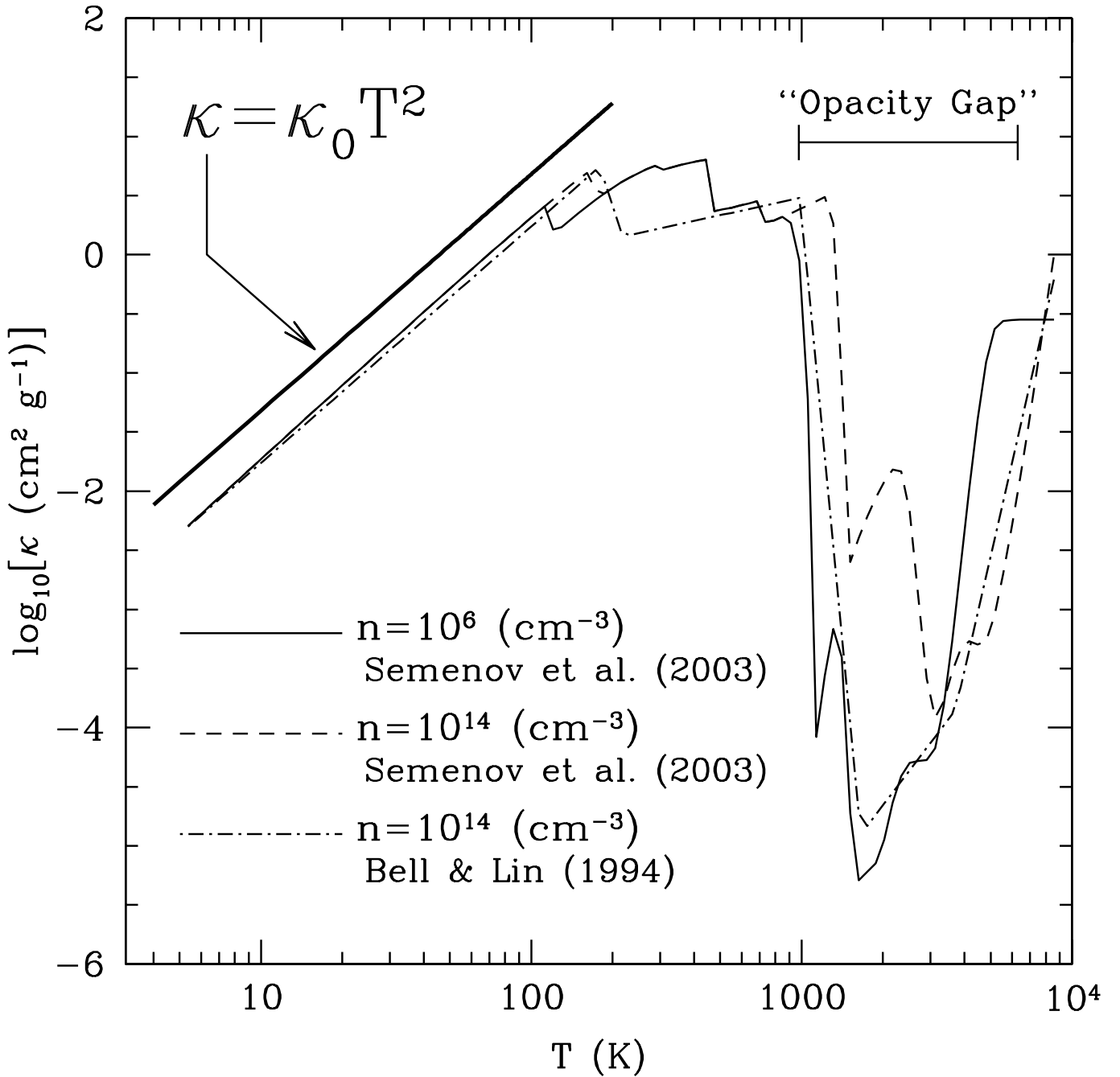


FIG. 1.— The Rosseland mean opacity as a function of temperature at several densities using two opacity models from the literature. Note the pronounced decrease in the opacity at the sublimation temperature of dust at $T \sim 1000$ K (the “opacity gap”). The rise in the opacity at higher temperature is due first to H-scattering, then to bound-free and free-free interactions, and finally to scattering off of free electrons. The thick solid line shows that at low temperatures, the opacity scales with the square of the temperature.

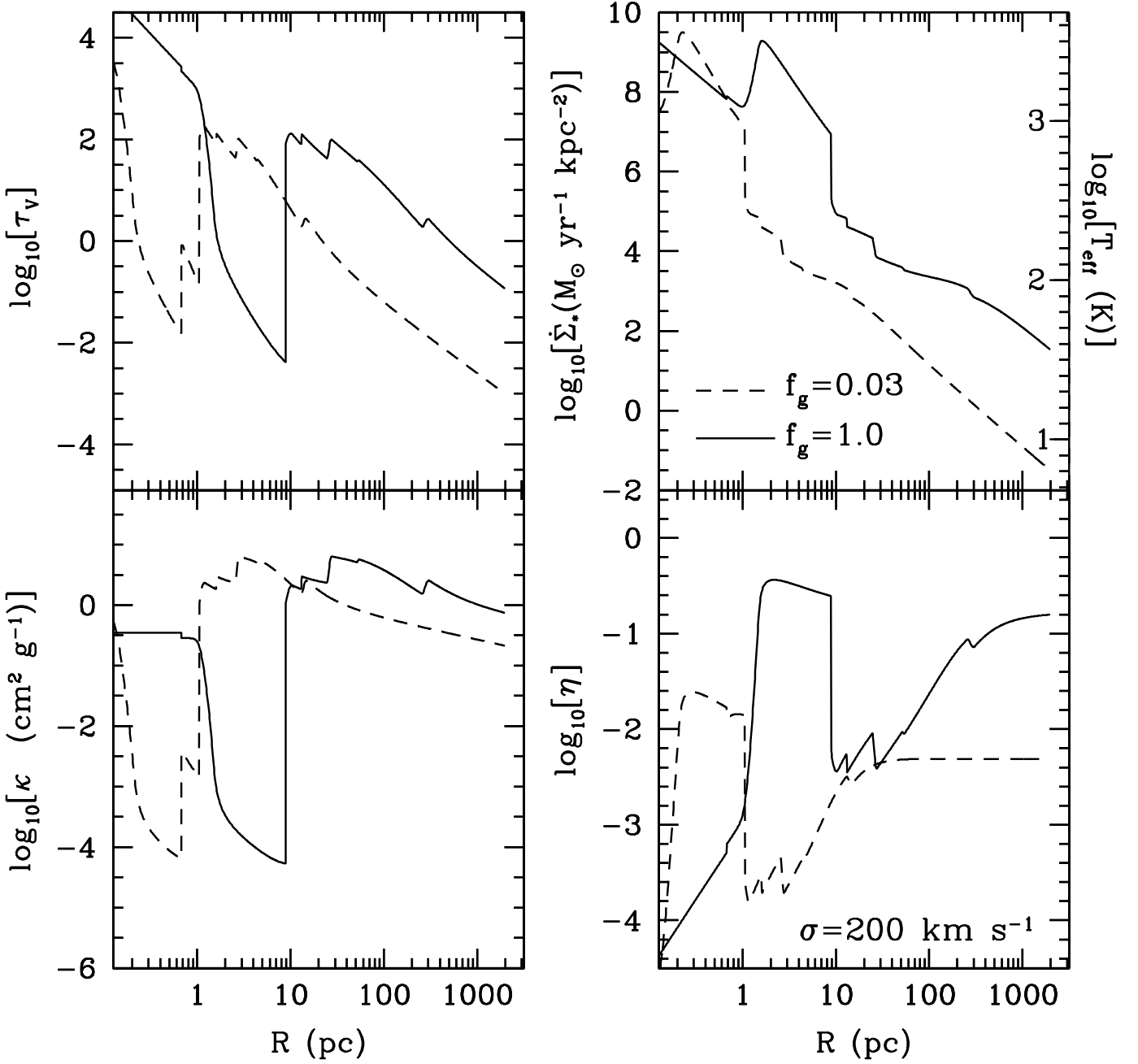


FIG. 2.— Vertical optical depth ($\log_{10}[\tau_v]$; upper left hand panel), opacity ($\log_{10}[\kappa (\text{cm}^2 \text{ g}^{-1})]$; lower left hand panel), star formation efficiency ($\log_{10}[\eta]$; lower right hand panel), and both the star formation rate per unit area and the effective temperature ($\log_{10}[\dot{\Sigma}_* (\text{M}_\odot \text{ yr}^{-1} \text{ kpc}^{-2})]$, $\log_{10}[T_{\text{eff}} (\text{K})]$; upper right hand panel) as a function of radius for models with $\sigma = 200 \text{ km s}^{-1}$ and either $f_g = 0.03$ (dashed line) or $f_g = 1$ (solid line). η approaches a constant for $r \gtrsim 100 \text{ pc}$ in the model with $f_g = 0.03$ when the disk is optically thin (see also eq. [18]). The model with $f_g = 1$ demonstrates that the star formation rate per unit area is roughly constant at intermediate radii $\sim 100 \text{ pc}$ (see §2.3). At small radii $\sim 0.01 - 10 \text{ pc}$, $\dot{\Sigma}_*$ is extremely large in the region where the dust sublimates and the opacity drops precipitously. Such large star formation rates are unphysical since the mass accreting through the starburst disk would quickly be exhausted. In §3 we construct more realistic models, taking into account the depletion of the gas locally as a result of star formation. Including this effect significantly reduces $\dot{\Sigma}_*$ on few-parsec scales (compare with Fig. 6).

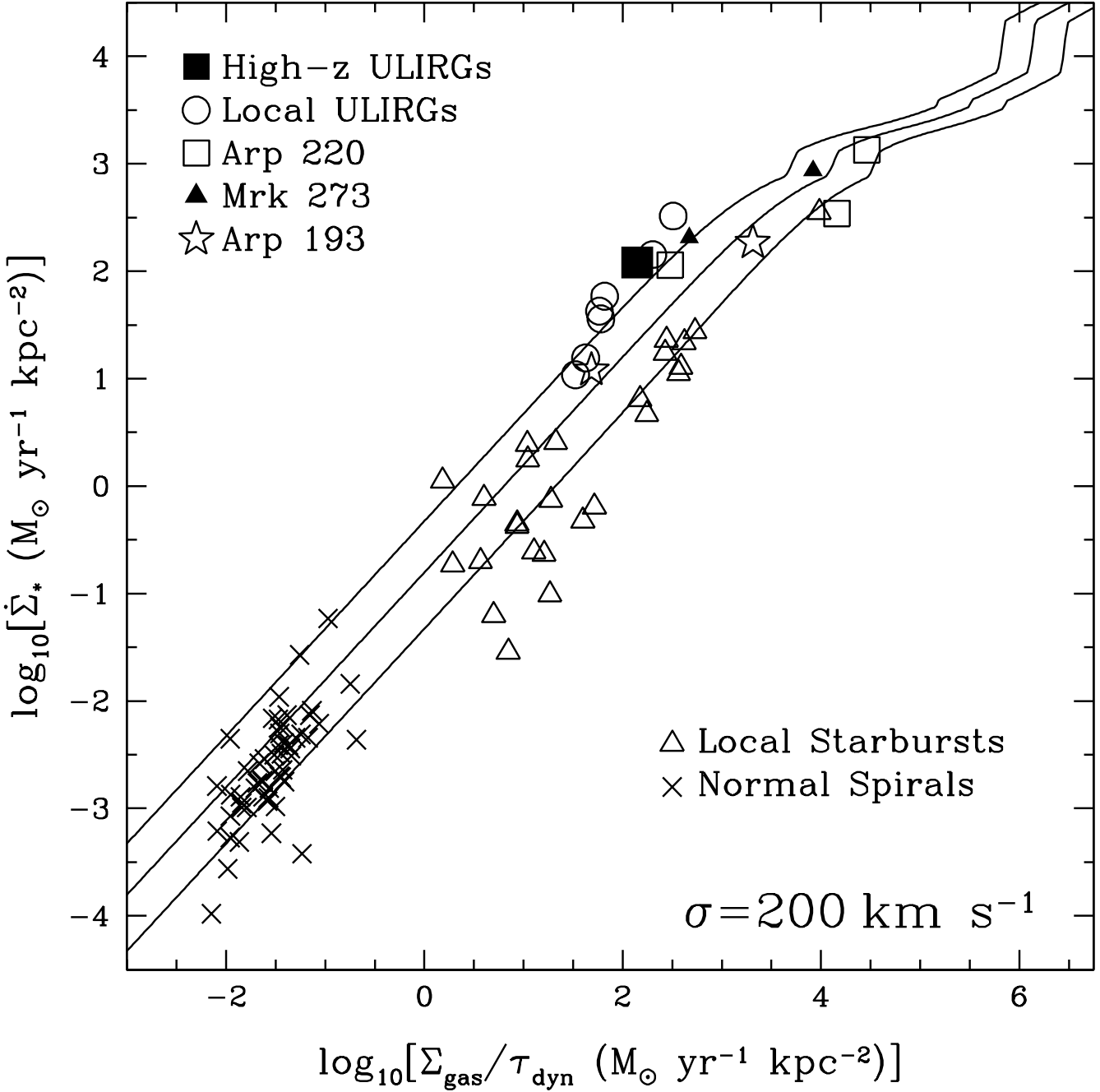


FIG. 3.— $\dot{\Sigma}_*$ as a function of $\Sigma_g/\tau_{\text{dyn}}$, where $\tau_{\text{dyn}} = 2\pi/\Omega$. This plot quantifies the star formation efficiency η (see eq. [8]). The solid lines show our model predictions, varying from the optically-thin limit (small $\Sigma_{\text{gas}}/\tau_{\text{dyn}}$) to the optically-thick limit (large $\Sigma_{\text{gas}}/\tau_{\text{dyn}}$). In the optically-thick limit $\eta \propto \kappa^{-1}$ and the sudden changes in $\dot{\Sigma}_*$ reflect sudden changes in κ (Fig. 1). For clarity of presentation, only models with $\sigma = 200 \text{ km s}^{-1}$ are shown for $f_g = 0.03, 0.1, \text{ and } 0.3$, despite the fact that the data have a variety of velocity dispersions. The data include normal star forming galaxies (crosses) and starburst galaxies (open triangles) from Kennicutt (1998). The filled square shows the average of the high- z ULIRGs from Tacconi et al. (2005). Local ULIRGs (open circles) are from Downes & Solomon (1998) with supporting data from other sources. These points use the “half-power” radius from Downes & Solomon’s Table 4, velocity dispersion inferred from their Table 5, and FIR luminosity taken from the text of Downes & Solomon (1998) (IRAS00057+4021, IRAS02483+4302, VII Zw 31) Genzel et al. (2001) (IRAS23365+3604, IRAS17208-0014), Heckman et al. (2000) (IRAS10565+2448), and Soifer et al. (2000) (Mrk 231). Arp 193 (stars), Arp 220 (open squares), and Mrk 273 (filled triangles) are plotted individually. The different points for the same source reflect the fact that Downes & Solomon distinguish between the outer CO disk and the inner “extreme” starburst nuclei (Table 12 of Downes & Solomon). For example, for Arp 220 we plot three separate points: the open square with $\log_{10}[\dot{\Sigma}_*] \approx 2$ and $\log_{10}[\Sigma_s/\tau_{\text{dyn}}] \approx 2.5$ corresponds to the large-scale $\sim 500 \text{ pc}$ CO disk, whereas the two open squares with $\log_{10}[\dot{\Sigma}_*/\tau_{\text{dyn}}] \approx 4$ and ≈ 4.5 correspond to the two compact ($\sim 100 \text{ pc}$) Arp 220 nuclei. Similarly, we plot two points for Mrk 273 and two points for Arp 193. The average of the high- z ULIRGs (filled square) and all of the local ULIRGs (open circles) employ a CO half-light or half-mass radius in the calculation of $\Sigma_g/\tau_{\text{dyn}}$ and $\dot{\Sigma}_*$. These quantities, thus inferred, are probably underestimates, since star formation appears to be significantly concentrated with respect to the CO (§2.5.1; Condon et al. 1991). This uncertainty corresponds to a horizontal and vertical shift of the open circles and the filled square similar in magnitude to that for Arp 220, Arp 193, and Mrk 273.

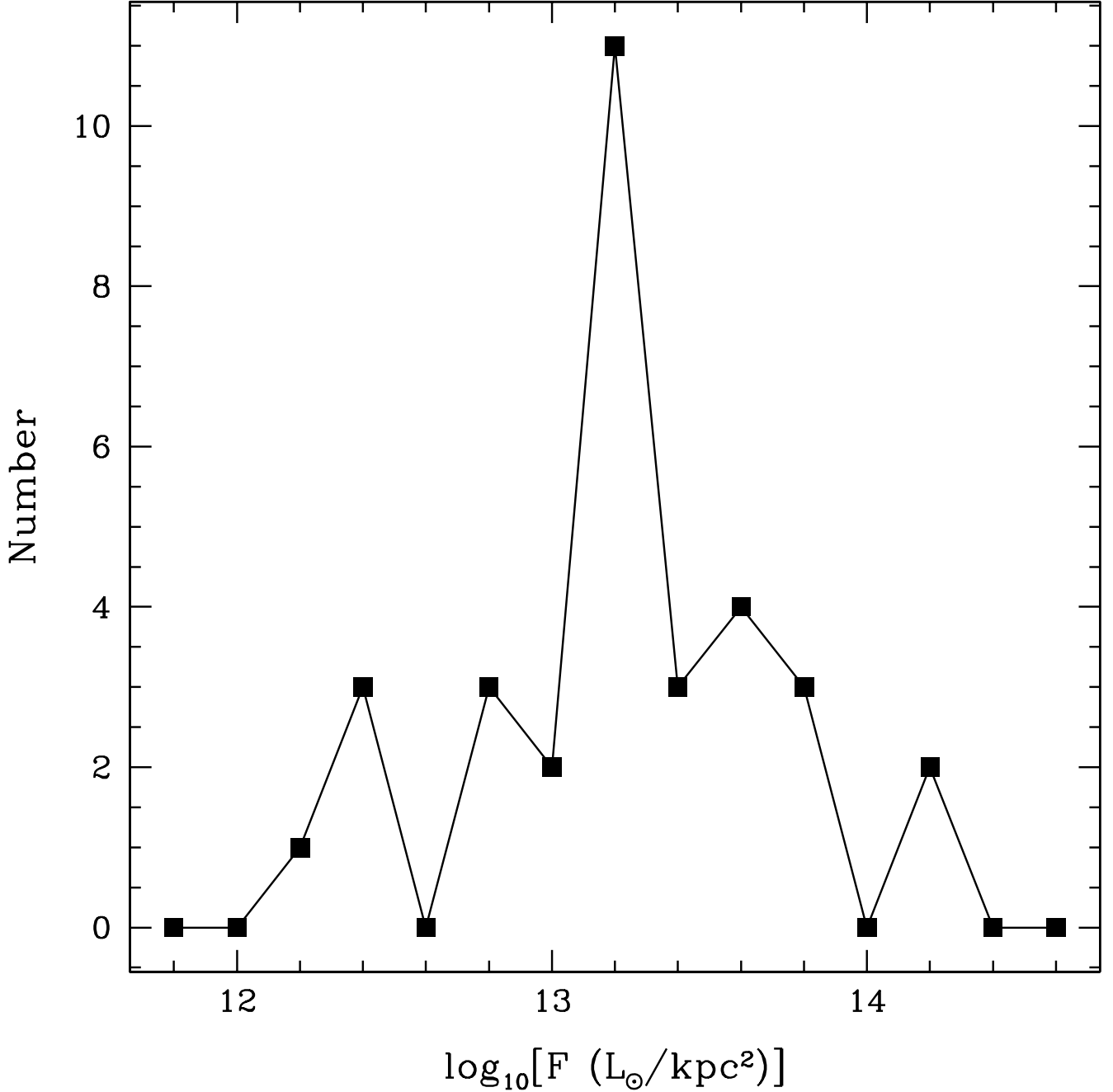


FIG. 4.— Histogram of the number of ULIRGs at a given flux using the sample in Tables 1 & 2 of Condon et al. (1991); the bins have a width of 0.2 in $\log_{10} F$. We estimate the intrinsic flux in the nuclear starburst using $F = L_{\text{FIR}}/A_{\text{radio}}$, where A_{radio} is the area of Condon et al.’s elliptical Gaussian fit to the radio emission; we exclude the 4 unresolved sources. The peak in the histogram at $\sim 10^{13} \text{ L}_\odot \text{ kpc}^{-2}$ is in good agreement with the predictions of our optically thick disk models (§2.3). See the text in §2.5.1 for uncertainties associated with using the radio size as a proxy for the starburst size.

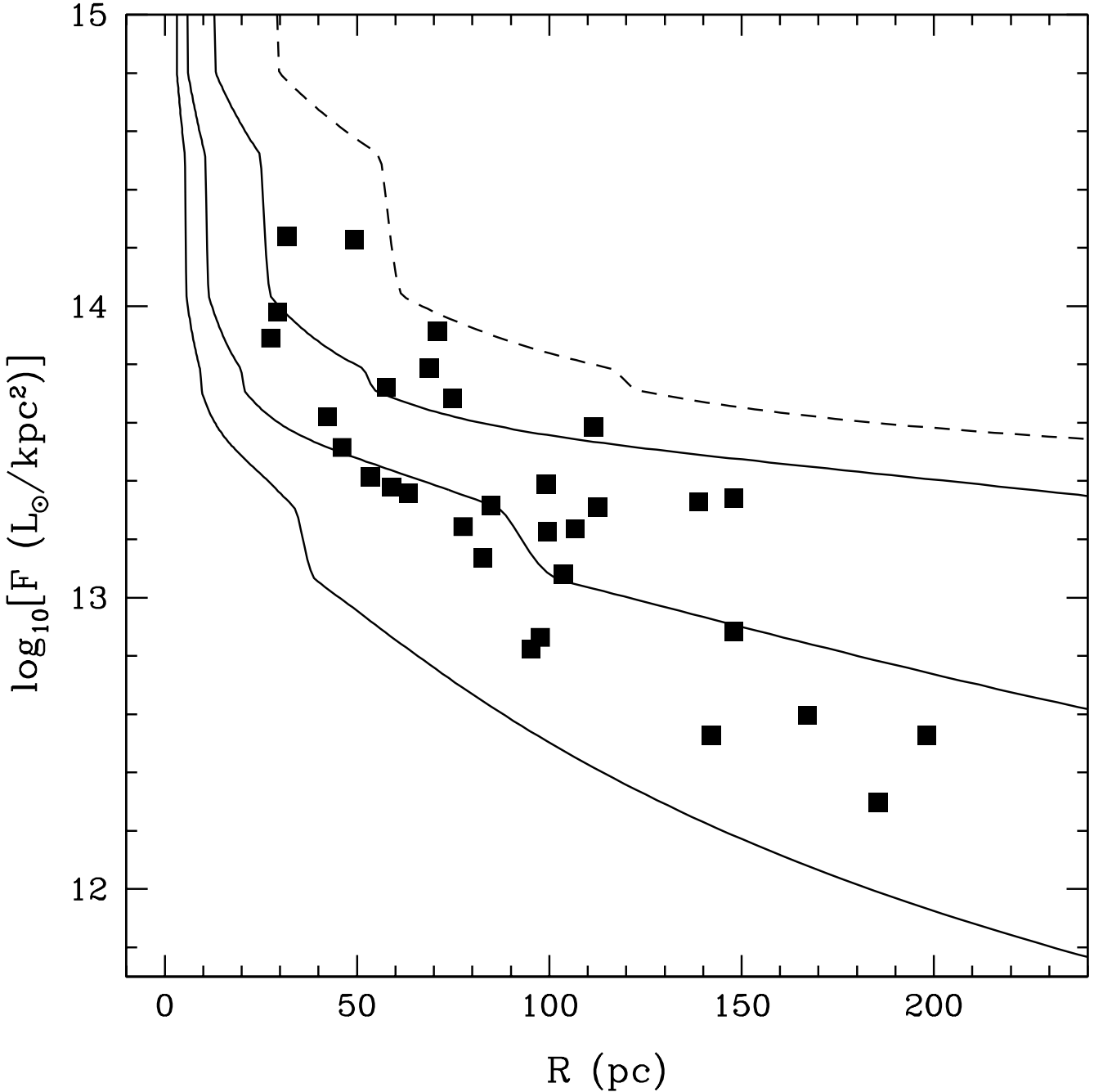


FIG. 5.— Flux as a function of radial scale for the local ULIRGs in Condon et al. (1991) (filled squares). The flux is inferred using $F = L_{\text{FIR}}/A_{\text{radio}}$, where A_{radio} is the area of Condon et al.'s elliptical Gaussian fit to the radio emission; we define the radial scale R by $A_{\text{radio}} \equiv \pi R^2$. The solid lines show results from our constant f_g models (compare with Figs. 2 & 3). From lowest to highest flux the models have $\sigma = 200 \text{ km s}^{-1}$ and $f_g = 0.1, 0.3, \text{ and } 1.0$ (solid lines). For comparison, the dashed line shows a model computed with $\sigma = 300 \text{ km s}^{-1}$ and $f_g = 1.0$.

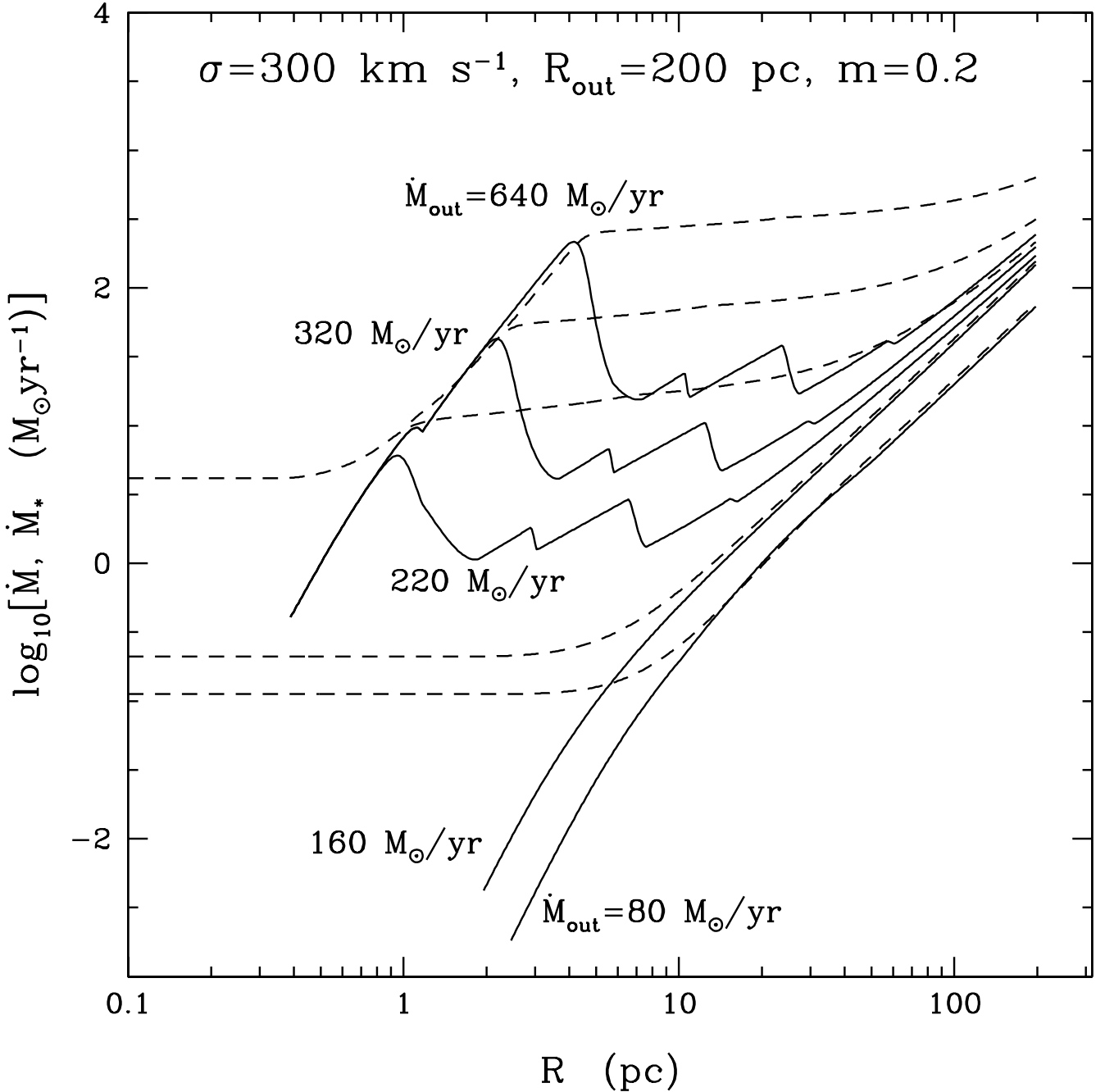


FIG. 6.— The local star formation rate ($\dot{M}_* = \pi r^2 \dot{\Sigma}_*$; solid lines) and accretion rate (dashed lines) as a function of radius for $\dot{M}_{\text{out}} = 80, 160, 220, 320$, and $640 \text{ M}_\odot \text{ yr}^{-1}$ in a model with $R_{\text{out}} = 200 \text{ pc}$ and $\sigma = 300 \text{ km s}^{-1}$. Note the strong bifurcation between models with low mass supply rates ($\dot{M}_{\text{out}} \leq 160 \text{ M}_\odot \text{ yr}^{-1}$; see eq. [44]) and models with high mass supply rates ($\dot{M}_{\text{out}} \geq 220 \text{ M}_\odot \text{ yr}^{-1}$). The latter produce outer ($r \sim R_{\text{out}}$) and inner ($r \sim 1 - 10 \text{ pc}$) starbursts, but also fuel a bright central AGN with $\dot{M}_{\text{BH}} \sim 4 \text{ M}_\odot \text{ yr}^{-1}$ (Appendix A). Figure 8 shows the computed spectra for each model. Figure 7 shows the full disk structure for the model with $\dot{M}_{\text{out}} = 320 \text{ M}_\odot \text{ yr}^{-1}$.

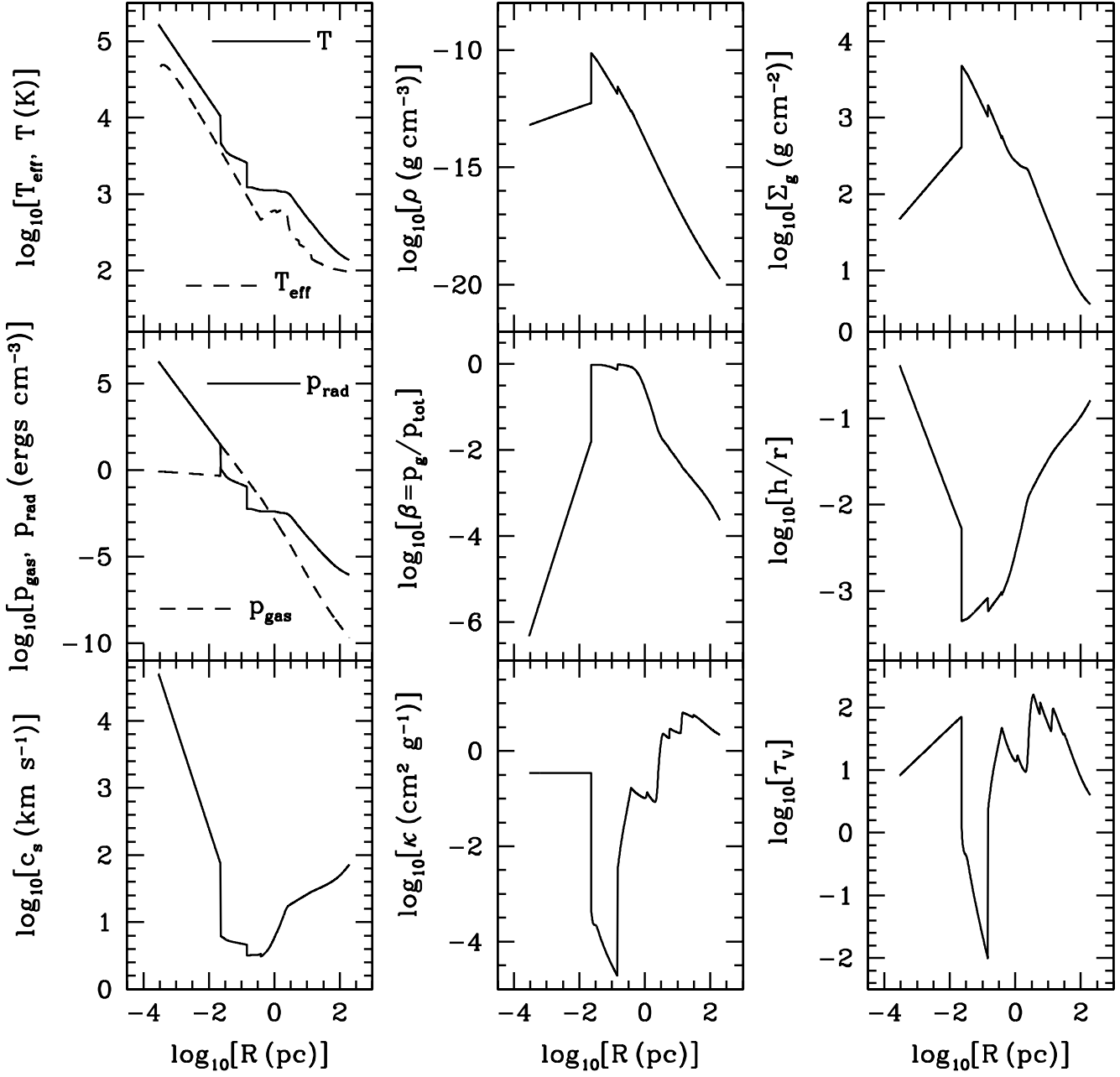


FIG. 7.— \log_{10} of T (solid line, upper left panel), T_{eff} (dashed line, upper left panel), ρ (upper middle panel), Σ_g (upper right panel), radiation pressure p_r (solid line, middle left panel), gas pressure p_g (dashed line, middle left panel), $\beta = p_g/p_{\text{tot}}$ (middle panel), h/r (middle right panel), c_s (lower left panel), κ (lower middle panel), and τ_v (lower right panel) all in cgs units as a function of radius in the model with $\dot{M}_{\text{out}} = 320 \text{ M}_\odot \text{ yr}^{-1}$, $R_{\text{out}} = 200 \text{ pc}$, and $m = 0.2$. The opacity gap region, highlighted in Figure 6, is located at $r \sim 1 \text{ pc}$.

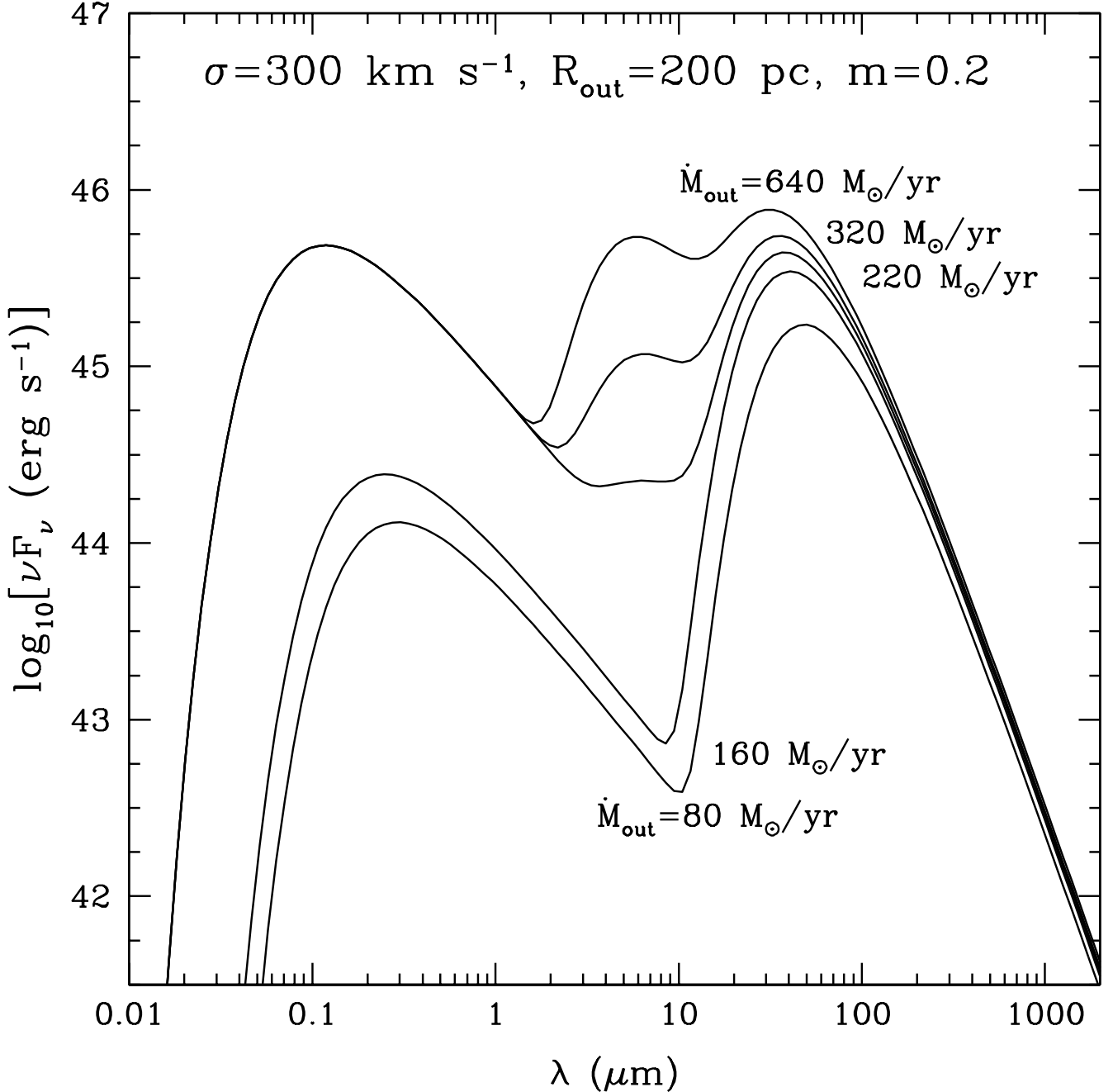


FIG. 8.— The spectral energy distribution as a function of wavelength for each of the disk solutions presented in Figure 6. Solutions with small mass supply rates ($\dot{M}_{\text{out}} \leq 160 M_{\odot} \text{ yr}^{-1} < \dot{M}_c$) are dominated by a starburst at large radii that produces a prominent FIR peak. Solutions with large mass supply rates ($\dot{M}_{\text{out}} \geq 220 M_{\odot} \text{ yr}^{-1} > \dot{M}_c$) have a similar FIR bump, but also have a spectral peak at $\sim 10 \mu\text{m}$ due to the inner ring of star formation in the opacity gap at 1–10 pc. As shown in Figure 6, these solutions also provide mass to the black hole at a rate comparable to the Eddington limit. The total bolometric emission from these models can be dominated by the central AGN, although there is a significant contribution from star formation (Appendix A).

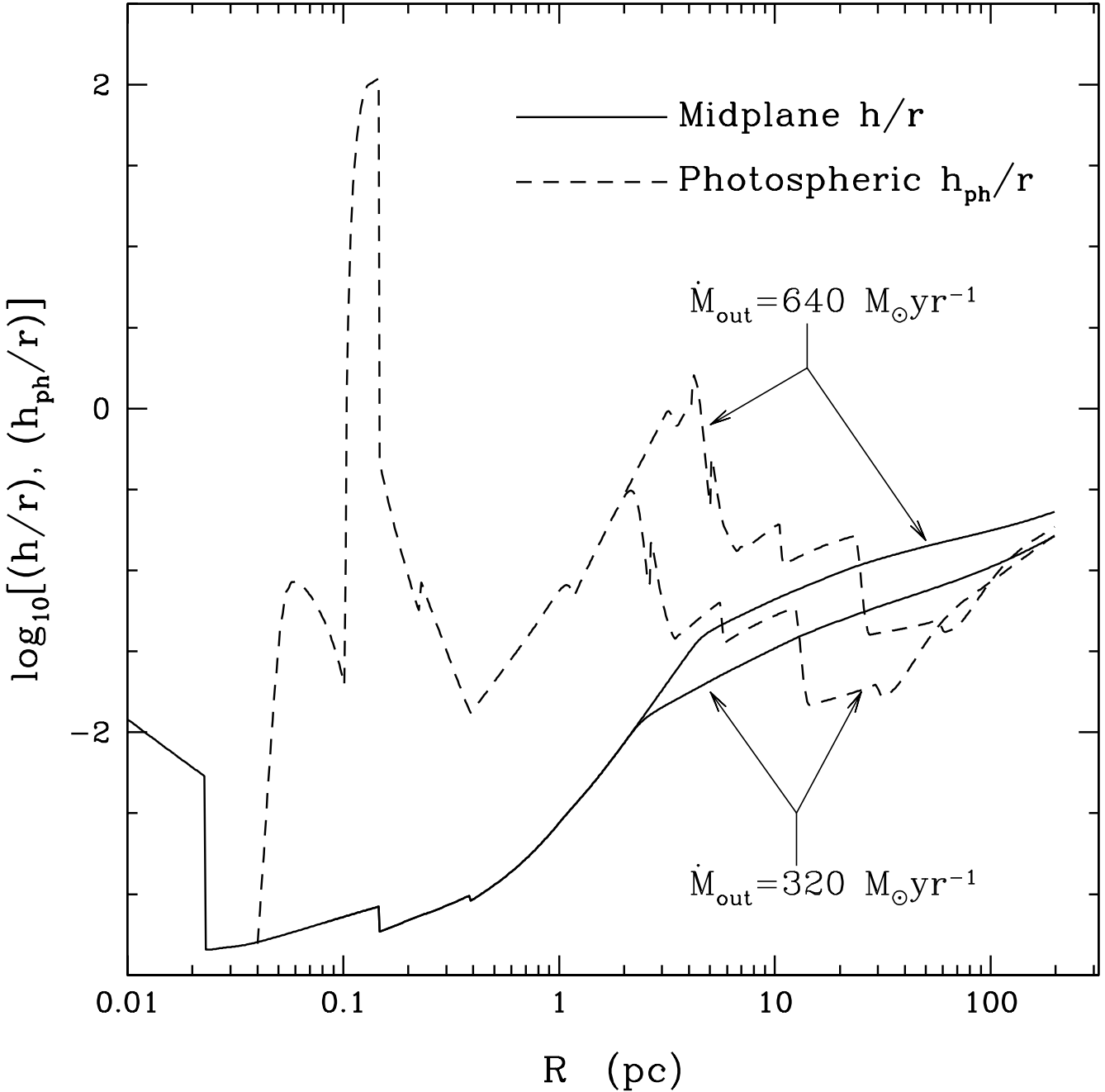


FIG. 9.— Estimates of the midplane (solid lines) and photospheric (dashed lines) scale-heights for two models with $\dot{M}_{\text{out}} = 320$ and $640 M_{\odot} \text{ yr}^{-1}$. The model with $\dot{M}_{\text{out}} = 640 M_{\odot} \text{ yr}^{-1}$ has higher midplane h/r at R_{out} and higher photospheric h_{ph}/r at $r \sim 10$ pc. Both models have the same midplane and photospheric scale height for $r \lesssim 2$ pc because of the power law solution in the opacity gap (Appendix A). Note that for $0.1 \lesssim r \lesssim 0.5$ pc the disk is gas pressure dominated at the midplane, but radiation pressure dominated at the photosphere (see Fig. 7). Values of $h_{ph}/r \gtrsim 1$ indicate that the photosphere is unbound.

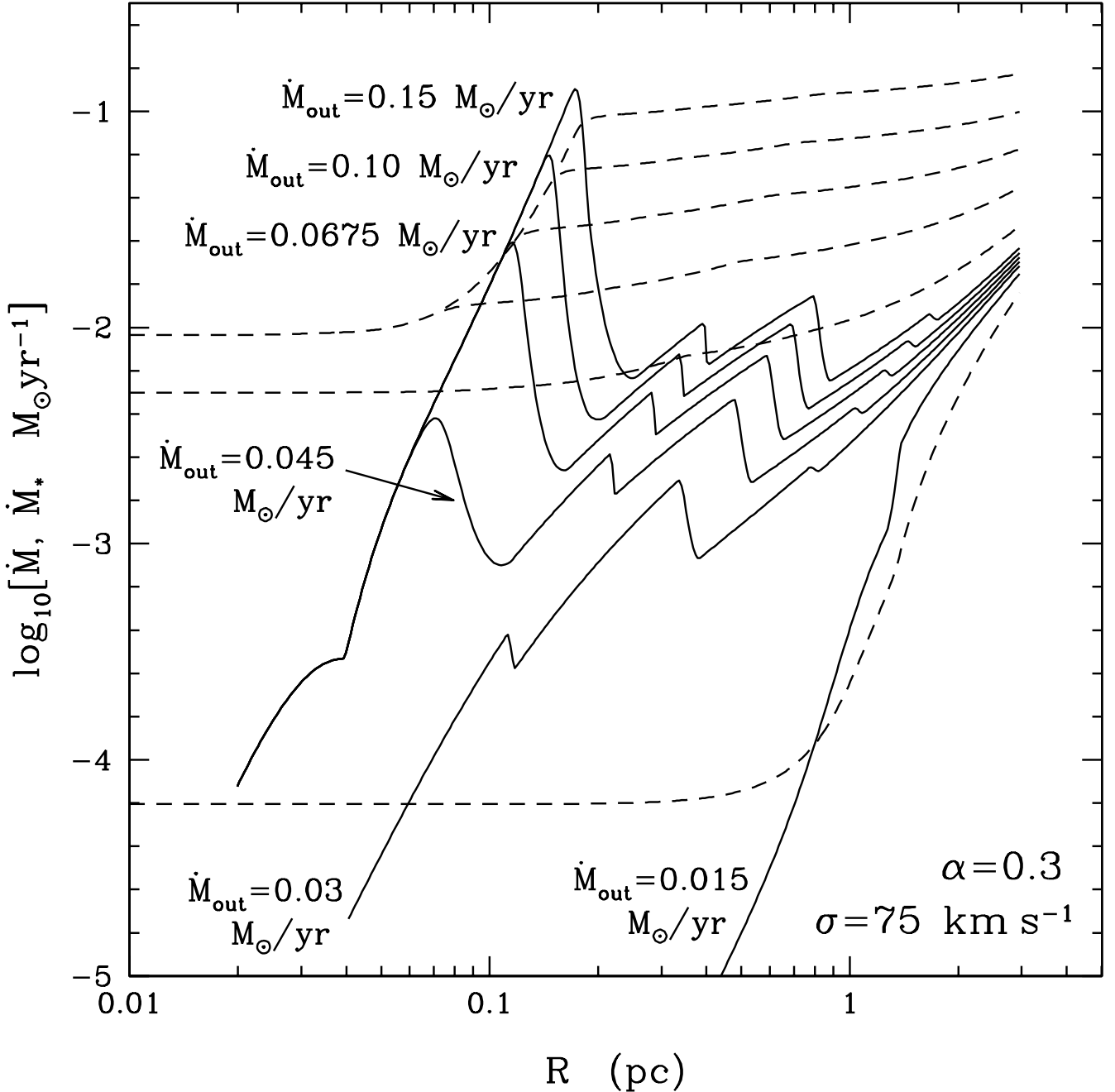


FIG. 10.— Star formation rate (solid lines) and gas accretion rate (dashed lines) in disk models appropriate to the Galactic Center ($M_{\text{BH}} = 4 \times 10^6 M_{\odot}$ and $\sigma = 75 \text{ km s}^{-1}$). We consider a mass supply rate \dot{M}_{out} at a radius $R_{\text{out}} = 3 \text{ pc}$ and accretion via a local α viscosity with $\alpha = 0.3$. The chosen values of R_{out} and \dot{M}_{out} are motivated by observations of the circumnuclear disk in the Galactic Center. Note that the opacity was increased by a factor of 3 relative to Figure 1 to account for the super-solar metallicity in the Galactic Center. These results show a ring of star formation at $\sim 0.1 \text{ pc}$ where there is currently a young disk of O and B stars.